

AD-A118 526

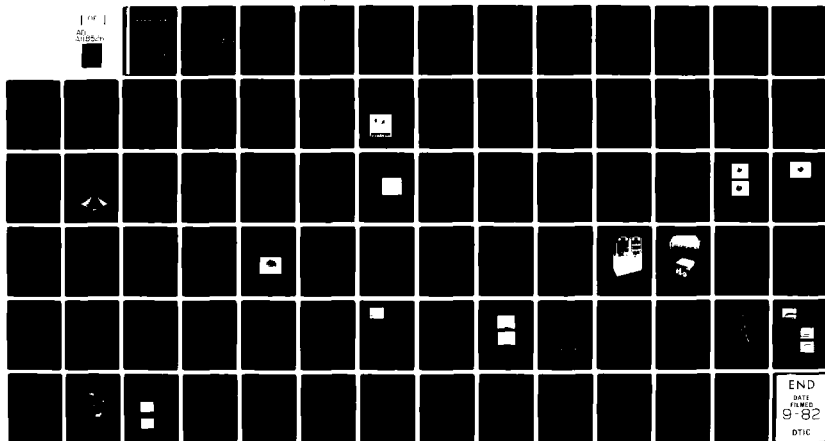
HUGHES RESEARCH LABS MALIBU CA  
MULTIDITHER ADAPTIVE ALGORITHMS.(U)  
JAN 77 R C LIND, K D PRICE, K M BROWN

F/6 17/8

F30602-76-C-0022

UNCLASSIFIED

NL



END  
DATE  
FILMED  
9-82  
DTIC

AD A118526

# MULTIDITHER ADAPTIVE ALGORITHMS

R.C. Lind, K.D. Price, K.M. Brown, T. Calderone, J.E. Pearson,  
S. Hansen, T.A. Nussmeier, and F.J. McClung

Hughes Research Laboratories  
3011 Malibu Canyon Road  
Malibu, CA 90265

January 1977

Contract F30602-76-C-0022

Interim Technical Report No. 3

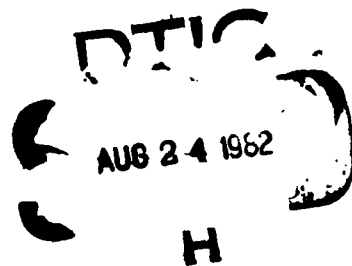
Mirror and Drive System Parameters and Performance

*Approved for public release; distribution unlimited*

DTIC FILE COPY

Prepared For  
DEFENSE ADVANCED RESEARCH PROJECTS AGENCY  
1400 Wilson Boulevard  
Arlington, VA 22209

Monitored By  
AIR FORCE SYSTEMS COMMAND  
Rome Air Development Center  
Griffiss Air Force Base, NY 13441



82 08 23 164

## UNCLASSIFIED

SECURITY CLASSIFICATION OF THIS PAGE (When Data Entered)

| REPORT DOCUMENTATION PAGE   |                       | READ INSTRUCTIONS<br>BEFORE COMPLETING FORM                                      |
|---|-----------------------|--|
| 1. REPORT NUMBER  | 2. GOVT ACCESSION NO. | 3. RECIPIENT'S CATALOG NUMBER  |
|   | AD-A118524            |  |
| 4. TITLE (and Subtitle)   |                       | 5. TYPE OF REPORT & PERIOD COVERED   |
| MULTIDITHER ADAPTIVE ALGORITHMS   |                       | Interim Technical<br>Report No. 3  |
|   |                       | 6. PERFORMING ORG. REPORT NUMBER   |
| 7. AUTHOR(s) R.C. Lind, K.D. Price, K.M.<br>Brown, T. Calderone, J.E. Pearson,<br>S. Hansen, T.A. Nussmeier, F.J. McClung   |                       | 8. CONTRACT OR GRANT NUMBER(s)<br><br>F30601-76-C-0022                           |
| 9. PERFORMING ORGANIZATION NAME AND ADDRESS<br>Hughes Research Laboratories<br>3011 Malibu Canyon Road<br>Malibu, CA 90265  |                       | 10. PROGRAM ELEMENT, PROJECT, TASK<br>AREA & WORK UNIT NUMBERS<br><br>PBA-6-1050 |
| 11. CONTROLLING OFFICE NAME AND ADDRESS<br>Defense Advanced Research Agency<br>1400 Wilson Boulevard<br>Arlington, VA 22209   |                       | 12. REPORT DATE<br>January 1977  |
| 14. MONITORING AGENCY NAME & ADDRESS (if different from Controlling Office)<br>Air Force Systems Command<br>Rome Air Development Center<br>Griffiss Air Force Base, NY 13441  |                       | 13. NUMBER OF PAGES  |
|   |                       | 15. SECURITY CLASS (of this report)<br><br>UNCLASSIFIED                          |
|   |                       | 15a. DECLASSIFICATION/DOWNGRADING<br>SCHEDULE                                    |
| 16. DISTRIBUTION STATEMENT (of this Report)<br><br>Approved for public release; distribution unlimited.   |                       |  |
| 17. DISTRIBUTION STATEMENT (of the abstract entered in Block 20, if different from Report)<br><br>DTIC<br>AUG 24 1982<br>H  |                       |  |
| 18. SUPPLEMENTARY NOTES<br>The views and conclusions in this document are those of the authors<br>and should not be interpreted as necessarily representing the official<br>policies, either expressed or implied of the Defense Advanced<br>Research Projects Agency or the U.S. Government.   |                       |  |
| 19. KEY WORDS (Continue on reverse side if necessary and identify by block number)<br><br>COAT, Thermal blooming Zernike, Deformable mirror   |                       |  |
| 20. ABSTRACT (Continue on reverse side if necessary and identify by block number)<br>A 37-element beryllium deformable mirror has been built, charac-<br>terized, and incorporated into a Coherent Optical Adaptive Technology<br>(COAT) system. Individual actuator deformation sensitivities of<br>0.2 $\mu\text{m}/150\text{ V}$ have been measured. Mirror resonance data has been<br>obtained indicating usable frequency ranges up to 30 to 40 kHz.<br>Strehl ratios approaching 80% have been measured for system defocus,<br>with COAT-off to COAT-on peak irradiance of 10. Auxiliary tracking |                       |  |

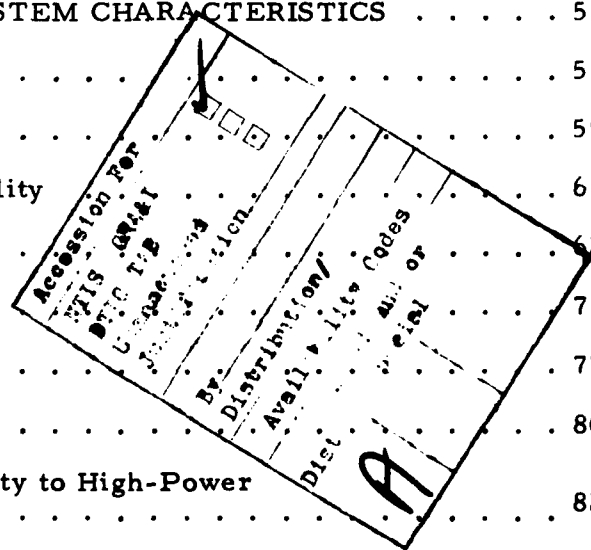
DD FORM 1473 1 JAN 73 EDITION OF 1 NOV 65 IS OBSOLETE

UNCLASSIFIED

SECURITY CLASSIFICATION OF THIS PAGE (When Data Entered)

## TABLE OF CONTENTS

|  |    |
|--|----|
| PREFACE . . . . .  | 5  |
| LIST OF TABLES . . . . .   | 7  |
| LIST OF ILLUSTRATIONS . . . . .  | 9  |
| SUMMARY . . . . .  | 13 |
| INTRODUCTION . . . . .   | 15 |
| Program Objectives . . . . .   | 15 |
| Research Program Plan . . . . .  | 15 |
| Organization of This Report . . . . .                                  | 16 |
| DEFORMABLE MIRROR MECHANICAL PROPERTIES . . . . .                      | 17 |
| Deformable Mirror Design and Construction . . . . .                    | 17 |
| Influence Function . . . . .   | 26 |
| Displacement Sensitivity . . . . .                                     | 39 |
| Surface Polish and Figure . . . . .                                    | 47 |
| Actuator Properties — Design Force and Voltage . . . . .               | 49 |
| Faceplate Design Considerations . . . . .                              | 49 |
| DEFORMABLE MIRROR COAT SYSTEM CHARACTERISTICS . . . . .                | 51 |
| Servosystem Description . . . . .                                      | 51 |
| Optical System Description . . . . .                                   | 59 |
| Mirror/Electronics Compatibility . . . . .                             | 61 |
| Performance Characteristics . . . . .                                  | 62 |
| HIGH POWER ASSESSMENT . . . . .  | 77 |
| Fabrication and Materials . . . . .                                    | 77 |
| Limitations . . . . .  | 80 |
| Summary of Design Applicability to High-Power Cooled Mirrors . . . . . | 82 |



|  |    |
|--|----|
| PLANS FOR REMAINDER OF CONTRACT . . . . .          | 83 |
| REFERENCES . . . . .                               | 85 |
| APPENDIX I - Mirror Profile Measurements . . . . . | 87 |

## PREFACE

This report was prepared by Hughes Research Laboratories, Malibu, California under contract F30602-76-C-0022. It describes work performed on Amendment No. 1 to the contract to characterize the deformable mirror. The principal investigator and principal scientist is Dr. Richard C. Lind. The project is part of the adaptive optics program in the Opto-Electronics Department, managed by Dr. Viktor Evtuhov, at Hughes Research Laboratories.

# LIST OF TABLES

| TABLE |   | PAGE |
|-------|---|------|
| 1     | RADC Deformable Mirror Performance Goals . . . . .  | 18   |
| 2     | Final Design Values . . . . .   | 24   |
| 3     | Servo Coupling Coefficients, $C_{sn}$ . . . . .   | 34   |
| 4     | Maximum Peak-Peak Surface Ripple for Hexagonal Actuator Array, Deformable Mirrors . . . . . | 36   |
| 5     | Actuator Peak Surface Deflection . . . . .  | 40   |
| 6     | Prominent Resonant Frequencies . . . . .  | 46   |
| 7     | Dither Frequencies for 19-Channel COAT System . . . . .                                     | 58   |
| 8     | COAT Servo Design Values . . . . .  | 58   |
| 9     | Material Stress Limitations . . . . .   | 81   |

RESEARCH PAGE BLANK-NOT FILMED

# LIST OF ILLUSTRATIONS

| FIGURE |   | PAGE |
|--------|---|------|
| 1      | Schematic of 37-actuator deformable mirror . . . . .  | 19   |
| 2      | Schematic of a single PZT actuator cell in the DARPA/RADC deformable mirror . . . . .   | 21   |
| 3      | Photograph of 37-element DARPA/RADC deformable mirror prior to final polishing . . . . .                                      | 22   |
| 4      | Schematic representation of deformable mirror parameters versus cell wall and faceplate thickness . . . . .                   | 25   |
| 5      | DARPA/RADC actuator location numbering guide . . . . .  | 27   |
| 6      | Influence function profiles of beryllium mirror . . . . .   | 28   |
| 7      | Influence function profile of beryllium mirror . . . . .  | 29   |
| 8      | RADC mirror faceplate influence function . . . . .  | 30   |
| 9      | Three-dimensional view of central-actuator influence for RADC beryllium mirror . . . . .                                      | 31   |
| 10     | Contour lines of measured profile of center actuator in DARPA/RADC mirror . . . . .   | 32   |
| 11     | Servo coupling and peak-peak ripple as a function of deformable mirror mechanical coupling . . . . .                          | 34   |
| 12     | Cross-sectional profiles of deformable mirror for three influence functions . . . . .   | 36   |
| 13     | Optimum value of exponent in order to produce minimum surface ripple . . . . .  | 37   |
| 14     | Experimentally observed surface profile with two adjacent actuators on DARPA/RADC mirror driven with equal voltages . . . . . | 37   |
| 15     | Experimentally observed surface profile with two adjacent actuators on beryllium mirror driven with equal voltage . . . . .   | 38   |



| FIGURE |   | PAGE |
|--------|---|------|
| 16     | Interferogram actuator No. 16 with +150 V<br>and zero voltage reference . . . . .                                   | 42   |
| 17     | Interferogram of all actuators on +150 V . . . . .  | 43   |
| 18     | Amplitude and phase reponse for central<br>actuator of beryllium mirror faceplate<br>thickness 0.125 in. . . . .    | 45   |
| 19     | Hysteresis plot for thin faceplate RADC<br>mirror . . . . .   | 47   |
| 20     | Optical surface figure after polishing . . . . .  | 48   |
| 21     | COAT system block diagram showing<br>additional multidither servo loops for<br>tracking and focus control . . . . . | 52   |
| 22     | (a) Signal conditioning electronics . . . . .   | 53   |
|        | (b) COAT servo electronics . . . . .  | 53   |
| 23     | Photograph of complete RADC/COAT control<br>electronics . . . . .   | 54   |
| 24     | Photograph of a 6-channel COAT electronics<br>panel . . . . .   | 55   |
| 25     | Focus and tracking controls . . . . .   | 55   |
| 26     | Piezo-electrically-driven, variable-radius<br>spherical mirror used for autofocus control . . . . .                 | 56   |
| 27     | Optical arrangement . . . . .   | 60   |
| 28     | Open loop gain/phase measurements 19<br>channel RADC mirror . . . . .   | 62   |
| 29     | Convergence time of COAT system . . . . .   | 64   |
| 30     | COAT performance . . . . .  | 64   |
| 31     | Beam profile . . . . .  | 66   |
| 32     | Formed array pattern, no turbulence . . . . .   | 67   |
| 33     | Relative convergence as a function of<br>PMT signal level . . . . .   | 68   |

| FIGURE |  | PAGE |
|--------|--|------|
| 34     | Deformable-mirror tracking of a moving<br>glint, no turbulence . . . . .   | 70   |
| 35     | Convergence time of tracking controls . . . . .  | 71   |
| 36     | PMT levels for initial level — no focus,<br>and initial level — with focus . . . . .                               | 71   |
| 37     | Deformable mirror plus auxiliary tracking<br>performance . . . . .   | 73   |
| 38     | Servo error signals occurring in a single<br>COAT control channel under conditions of<br>high turbulence . . . . . | 74   |

## SUMMARY

The objective of this program on coherent optical adaptive techniques (COAT) is to investigate algorithms and techniques that can reduce the beam distortions caused by thermal blooming. This Interim Report No. 3 is devoted entirely to a discussion of the supplemental task, Task 4: Mirror and Drive System Parameters and Performance. A description of the previous work on the contract can be found in Interim Reports 1 and 2.<sup>1</sup>

A 37-element, all-beryllium deformable mirror has been designed and constructed under this contract. Only 19 of the 37 elements are in use due to the inability of the supplier to deliver all of the mirror actuators during the contract period. This report is addressed to a description of the characterization of this 19-element mirror.

Tests on the mirror have determined its influence function, excursion sensitivity, surface figure, hysteresis, and frequency response. On the average, each actuator delivers  $0.2 \mu\text{m}$  of surface motion for about 150 V of drive, close to the design value of  $0.26 \mu\text{m}$ . The frequency response shows resonances in the 12 to 15, 18 to 20, and 24 kHz range. With appropriate scaling of the COAT electronics for the actuator response in those frequency ranges, the COAT system operates quite favorably. The influence function has a shape dependent upon the faceplate thickness and is given by  $IN(r) = \exp(-Br^{1.5})$  for a 0.15 in. thickness and by  $\exp(-cr^{1.71})$  for a thinner faceplate of 0.125 in. The mechanical coupling coefficients are 23% and 14% respectively. The thin faceplate has been shown to have desirable coupling coefficient-to-surface ripple tradeoff and is used for the COAT performance experiments.

Using the thin faceplate deformable mirror in the COAT system, initial performance data were obtained. Loop gain and phase measurements indicated expected gain and phase stability margins. Convergence times as short as 1.5 msec were measured and the effect of initial conditions on convergence established. Strehl ratios approaching 80% were obtained for defocused beams with a COAT-OFF to COAT-ON peak irradiance of 10. Tracking limits of 3 to 4 diffraction limited beam diameters were measured for the deformable mirror. The auxiliary tracking and focus controls were implemented with

the deformable mirror and the interaction of the various systems was analyzed. The existence of " $2N\pi$ " states for the deformable mirror COAT system was demonstrated.

During the remainder of the contract the deformable mirror COAT system will be employed in both the standard zonal COAT mode and in a Zernike polynomial modal mode to investigate compensation of thermal blooming. Results of this investigation will be published in the final report.

## INTRODUCTION

### PROGRAM OBJECTIVES

The primary objective of this program on coherent optical adaptive techniques (COAT) is to analyze and experimentally demonstrate adaptive multidither correction algorithms that can reduce beam distortions caused by thermal blooming. In addition, the use of fixed transmitter intensity profiles for reducing thermal blooming is being investigated.

### RESEARCH PROGRAM PLAN

The research program utilizes the DARPA/RADC experimental COAT system built and tested on contracts F30602-73-C-0248 and F30602-75-C-0001. Computer simulation codes developed on these contracts and on other programs (e. g. , NSWC contract N60921-74-C-0249) are being used for the analytical portions of this contract. These codes model the operation of several types of COAT servomechanisms as well as the time-dependent propagation of optical beams in an absorbing and turbulent medium. The experimental investigations require construction of a deformable mirror for the COAT system as part of the program.

To accomplish the objectives of this contract, a 12-month research program consisting of three major tasks was developed. Task 1 is an analytical task and is partially completed. Task 2 provides for the construction of a deformable mirror and is completed. In Task 3 the mirror is used to study thermal blooming compensation with zonal multidither control and with modal control using Zernike-polynomial modes. Work on this task is in progress.

Amendment No. 1 to the contract has provided funds to characterize the beryllium deformable mirror that has been built and to assess the applicability of this design to high-power laser COAT systems. The characterization of the mirror is complete and is the subject of this report.

## ORGANIZATION OF THIS REPORT

This report is devoted entirely to a discussion of the characterization of the DARPA (RADC) beryllium deformable mirror.

The second section discusses the deformable mirror mechanical properties. In particular, it presents a summary of the design goals for the mirror together with a description of the influence function, displacement sensitivity, surface polish, actuator properties, and faceplate considerations for the mirror.

The third section describes the deformable mirror COAT system characteristics. It also describes the COAT system hardware coupled to the deformable mirror. The performance of the COAT system employing the deformable mirror is discussed in detail.

The fourth section discusses the applicability of the design of deformable mirrors to high power situations.

The fifth section presents a brief discussion of the remainder of work to be done on the contract.

## DEFORMABLE MIRROR MECHANICAL PROPERTIES

This section will present a description of the design goals and features of the deformable mirror together with a detailed presentation of experimental and analytical characterizations.

### DEFORMABLE MIRROR DESIGN AND CONSTRUCTION

#### Mirror Performance Goals

The mirror built on this contract replaces the beam-splitter/phase-shifter array (called the "phasor matrix") that has been used successfully up to now with the DARPA/RADC COAT system. It performs the two functions of phase dithering (tagging) and phase correction required in any type of multidither COAT system. Performance of both these functions with a single element places heavy and conflicting demands on the device. The phase correction function requires large-amplitude phase excursions (about 2 optical wavelengths) at relatively low frequencies (up to about 1 kHz). On the other hand, the dither function requires small-amplitude excursions ( $30^\circ$ ) at much higher frequencies (10 to 30 kHz). To date, no continuous-surface, deformable mirror device has ever been constructed that can accomplish both of these functions simultaneously, particularly with the low drive voltages ( $\pm 150$  V) available from the DARPA/RADC COAT system.

The mirror built on this program is the first of a kind and as such will represent the state of the art for uncooled deformable mirrors of its type. Because such a mirror had not been built, or even designed previously, an extensive design effort was initiated. This design has been funded only in part by this contract, the remainder of the work being performed as part of the Hughes Aircraft IR&D program.

The design and analysis effort started with Hughes-proprietary designs for a multielement deformable mirror and for external-spring, self-contained piezoelectrically driven actuator cells. The performance goals of the design are listed in Table 1. The number of actuators was set by a compromise between available funds and the number of actuators required to produce the first 7 to 10 Zernike polynomials (for thermal blooming compensation

studies to be carried out during this contract). Beryllium was chosen as the structural material because of its large stiffness-to-weight ratio and reasonably low thermal expansion coefficient compared to molybdenum or aluminum. The structural resonant frequencies should be about  $\sqrt{6}$  higher when using beryllium instead of molybdenum in a given design.

TABLE 1. RADC DEFORMABLE MIRROR PERFORMANCE GOALS

| Performance Characteristic | Value   |
|----------------------------|---|
| Faceplate excursion        | $\pm 0.5 \mu\text{m}$ ( $\pm 2\lambda$ phase shift at $\lambda = 0.488 \mu\text{m}$ ) with $\pm 150$ V of drive |
| Surface flatness           | $\lambda/2$ overall; $\lambda/6$ over any localized actuator area   |
| Frequency response         | In excess of 10 kHz, but as high as possible  |
| Structure material         | Beryllium   |
| Piezoelectric material     | Gulton 6-1512   |
| Number of actuators        | 37 in a circular arrangement  |
| Mirror surface             | Solid, uncooled   |
| Actuator cooling           | Not required for visible wavelength operation   |

T1795

#### Mirror Design Features

A schematic of the mirror is shown in Figure 1. The entire mirror body is made of beryllium. The 37 actuators are placed on a circular array with a minimum actuator spacing of 0.550 in. The active mirror surface has a diameter of 3.980 in. The faceplate is initially 0.055 to 0.060 beryllium stock, and is butt brazed to each of the 37 actuators and to the rim of the primary backup. The faceplate will be polished and coated with protected silver. The actuator cells are brazed to the primary backup at the same time as the faceplate braze.



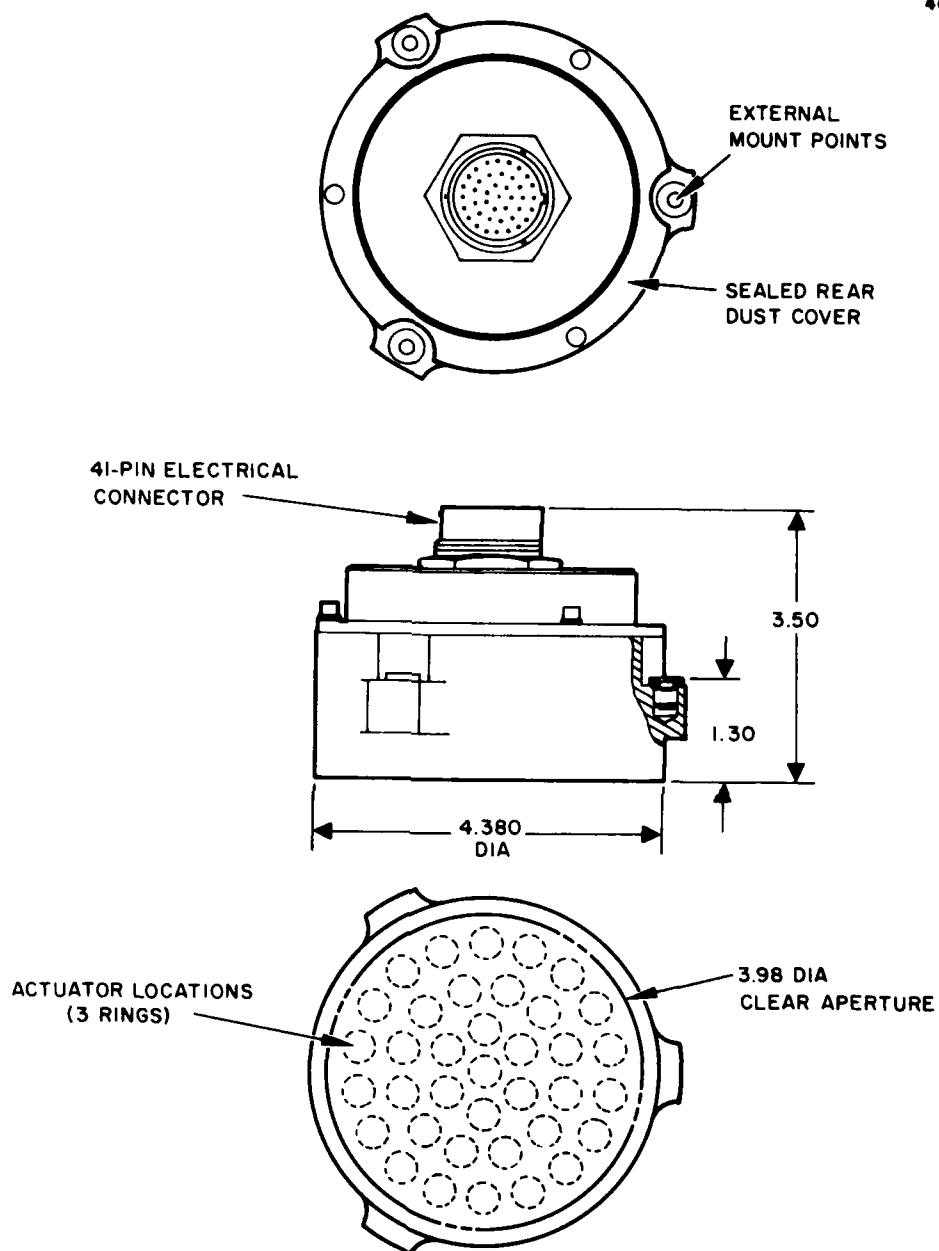


Figure 1. Schematic of 37-actuator deformable mirror.

Each mirror actuator is composed of a cylindrical spring assembly which houses a stack of 19 piezoelectric annular washers. A schematic of a single cell is shown in Figure 2. Each washer is 0.024 in. thick, made of Gulton 6-1512 material. The cell is attached to the backup structure so that its entire length is effective in producing surface motion.

The transducer stack is electrically grounded at the mirror faceplate and the driver voltage is applied through the electrode at the other end of the PZT stack. With this arrangement, the transducer stack is internally wired, thus eliminating the complication of feeding wires out from the stack. The only wire to each actuator is conveniently soldered to the electrode in a manner that directs the wire straight out of the cell, with no bends requiring additional volume. This electrical arrangement is compatible with the electronics of the DARPA/RADC electronics, which has a common ground for all channel outputs. All of the electric outputs are brought to a 41-pin electrical connector that is attached to the dust cover at the back of the mirror (see Figure 2).

Each stack is preloaded to a nominal value of 32 lb. This is accomplished by torquing a preload screw to 30 to 35 in.-oz. The preload screw bears against an antirotation washer so that torque is not transmitted to the transducer. A photograph of the completed unit is shown in Figure 3.

#### Mirror Performance Analysis

An important area of design investigation has been the response of the mirror body to unbalanced actuator excitation. The amplitude of response of the mirror backup is proportional to the magnitude of the unbalanced forces in the actuators. For a beryllium structure, the unbalanced forces are derived almost entirely from the relatively massive PZT stacks. This force can be calculated by using

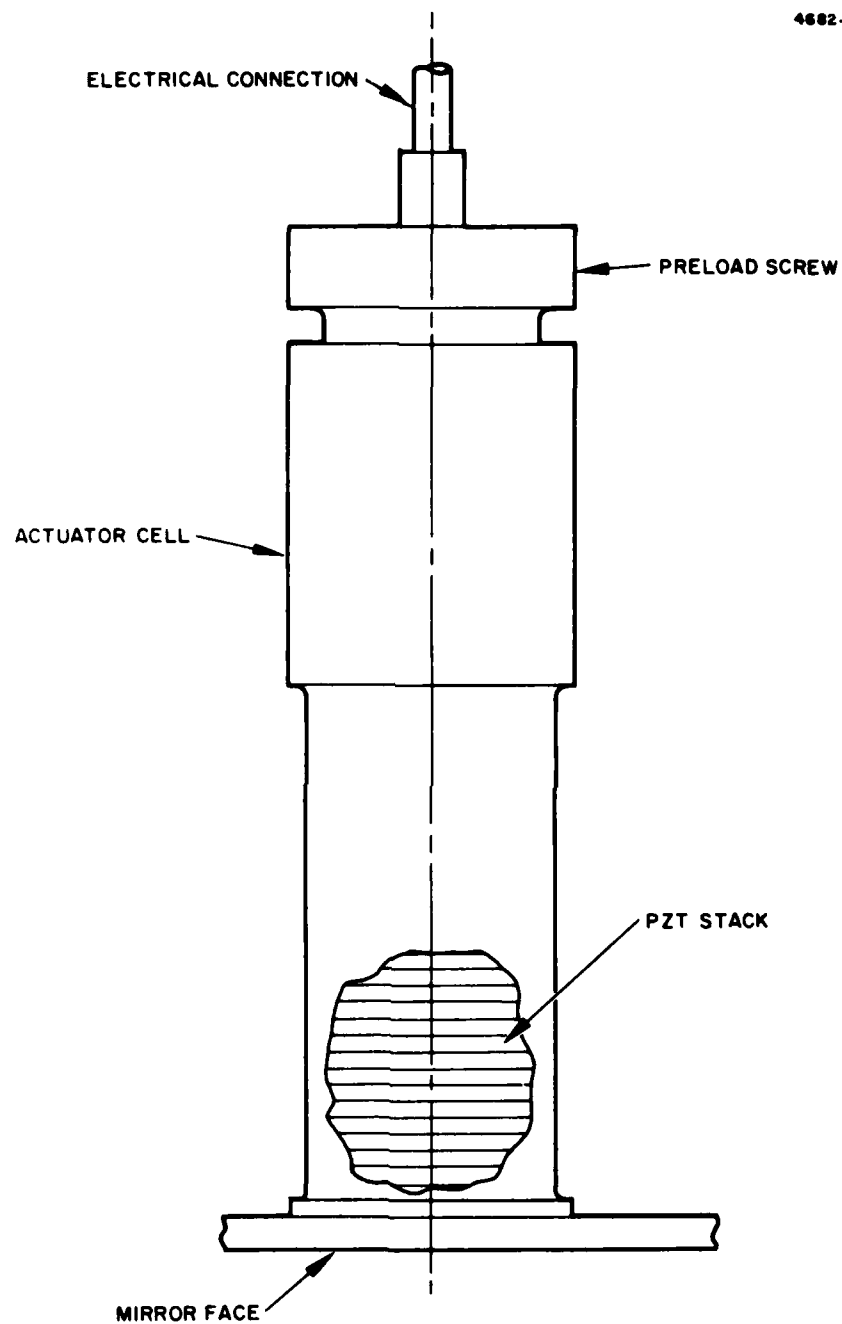


Figure 2. Schematic of a single PZT actuator cell in the DARPA/RADC deformable mirror.

$$F_{rms} = \pi^2 \sqrt{2} \frac{w}{g} u f^2 \quad (1)$$

where  $w$  is the weight of PZT stack and cell,  $g$  is the acceleration of gravity,  $u$  is the maximum excursion of mirror, and  $f$  is the driving frequency.

A 1/4 in. -diameter actuator weighs about 0.010 lb, and the required dither motion is about 2  $\mu$ in. The rms force is therefore  $F_{rms} \approx 7.2 \times 10^{-10} f^2$  lb. At 15 kHz, the force is 0.163 lb. Assuming an amplification factor ( $Q$ ) of 10 for the beryllium mirror at the 20 kHz resonance (see Figure 18) and a limit of 0.2  $\mu$ in. due to structural vibrational motion, the mirror must have a stiffness of at least

$$K = \frac{QF}{u} = \frac{(10)(0.146)}{(0.2 \times 10^{-6})} \text{ lb/in.} = 8 \times 10^6 \text{ lb/in.}$$

Our analysis indicates that the stiffness of the mirror (referenced to a load at the center actuator) is of the order of magnitude  $10^7$  lb/in. Thus, for actuators driven near natural frequencies, it is not expected that mirror performance will be greatly degraded by unbalanced actuators.

5353-21

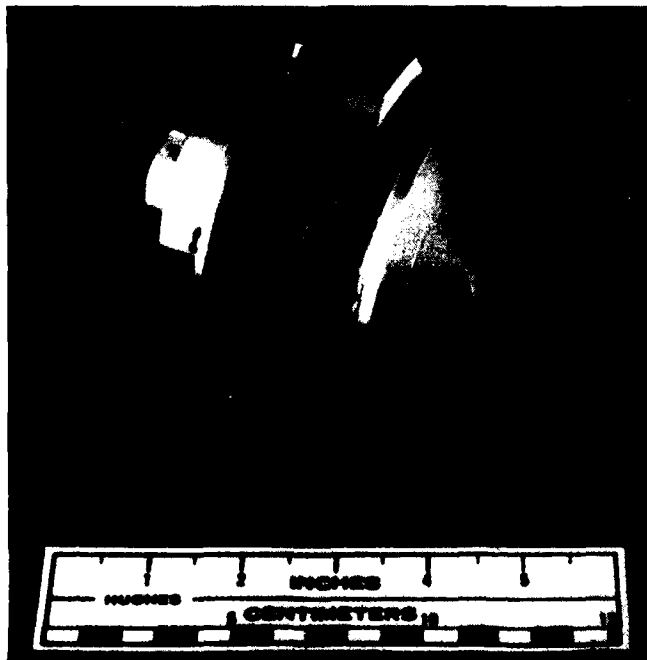


Figure 3.  
Photograph of 37-element  
DARPA/RADC deform-  
able mirror prior to  
final polishing.

The final major design consideration was the tradeoff among faceplate thickness, resonant frequencies, mirror motion, and number of PZT washers in each actuator cell. The motion,  $u$ , of the mirror surface may be described by

$$K_A \geq \frac{K_B}{\frac{\eta \delta_F}{u} - 1} \quad (2)$$

$$\eta \geq \frac{u}{\delta_F} \frac{(K_A^{-1} + K_B^{-1})}{K_B^{-1}} \quad (3)$$

$$K_A^{-1} = K_P^{-1} + (\eta + 1)K_e^{-1} + K_s^{-1} \quad (4)$$

where

$K_A \equiv$  Transducer assembly stiffness (lb/in.)

$K_B \equiv$  Actuator cell plus faceplate stiffness (lb/in.)

$\eta \equiv$  Number of active PZT washers

$\delta_F \equiv$  Free expansion of one PZT washer (in.)

$= d_{33} \Delta V$

$d_{33} \equiv$  Piezoelectric charge coefficient (in./V)

$\Delta V \equiv$  Applied voltage (V)

$u \equiv$  Motion of mirror surface (in.)

$K_P \equiv$  Stiffness of one PZT washer

$K_e \equiv$  Stiffness of one electrode

$K_s \equiv$  Total stiffness of all remaining elements in transducer stack.

Since in most mirror applications  $u$  is defined, equations (2) to (4) can be rearranged into a more useful form to give the minimum required number of washers,  $\eta$ :

$$\eta \geq \frac{u/\delta_F(K_B^{-1} + K_e^{-1} + K_s^{-1})}{K_B^{-1} - u/\delta_F(K_P^{-1} = K_e^{-1})} \quad (5)$$

Equation (5) has been solved parametrically for a number of PZT dimensions and materials. The design values chosen are listed in Table 2.

Based on these design tradeoffs we can identify several trends for the mirror parameters, assuming that we want to maximize frequency response and minimize thermal distortions and mechanical stresses. The trends are shown in Figure 4. (The curves should be viewed relative to the ordinate and abscissa axes, not with respect to each other.)

TABLE 2. FINAL DESIGN VALUES

| Design Parameter       | Value                    |
|------------------------|--------------------------|
| $\eta$                 | 29                       |
| $K_B$                  | $0.9 \times 10^6$ lb/in. |
| $K_{\text{cell}}$      | $0.7 \times 10^6$ lb/in. |
| $K_{\text{faceplate}}$ | $0.2 \times 10^6$ lb/in. |
| $K_e$                  | $8.0 \times 10^8$ lb/in. |
| $K_s$                  | $10^7$ lb/in.            |
| PZT Washer:            |                          |
| Outside Diameter       | 0.255 0.005              |
| Thickness              | 0.0235 0.001             |
| Material               | G-1512                   |

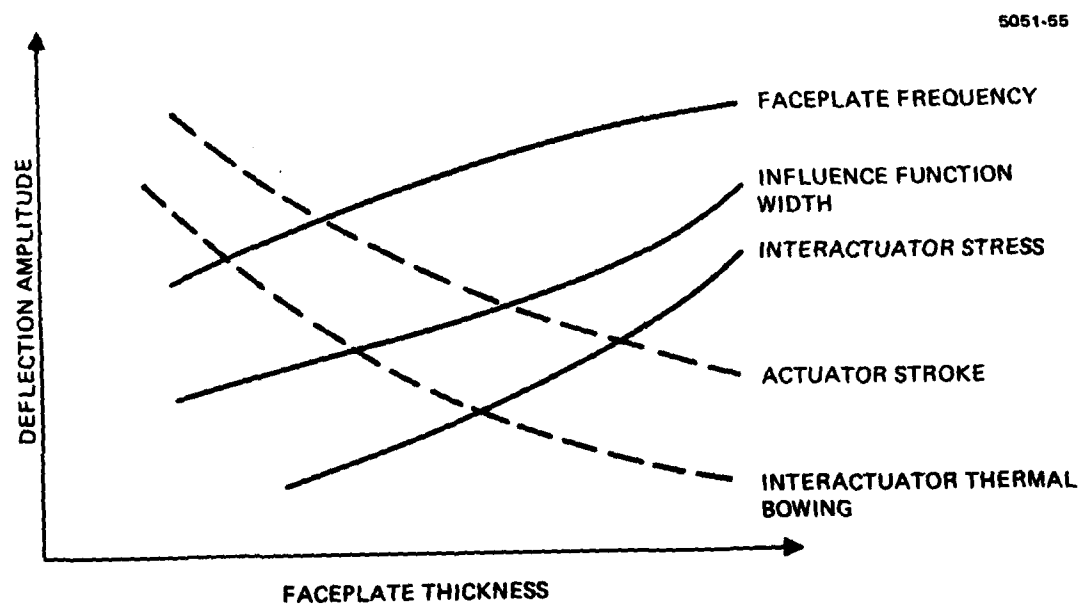
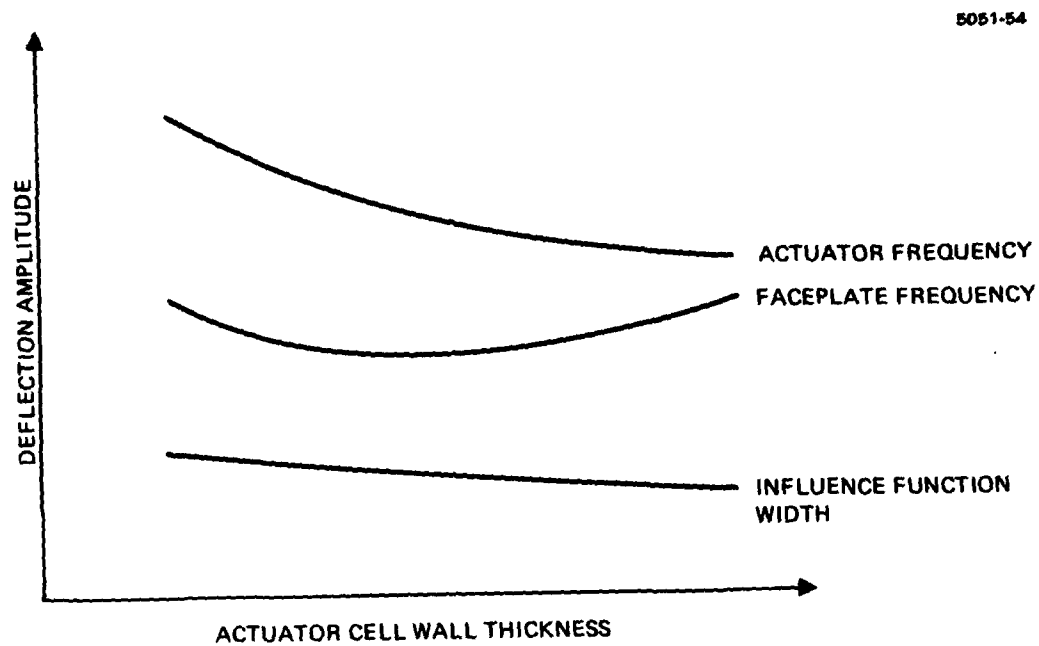


Figure 4. Schematic representation of deformable mirror parameters versus cell wall and faceplate thickness.

## INFLUENCE FUNCTION

The influence function determines two very important quantities: the servo-channel cross coupling (when each mirror actuator is driven by a single servochannel), and the interactuator mirror surface "ripple" when several actuators are driven with near-equal amplitudes. A detailed analytic and experimental effort has been undertaken to characterize the influence function for the RADC mirror.

### Measurements and Correlations

Influence functions have been measured for two faceplate thicknesses. A thick faceplate (0.150 in.) prior to polish and a thin faceplate configuration (0.125 in.) after polish.\* For the thick configuration, measurements were made for an actuator in each of the three rings plus the center actuator. For the thin configuration, profiles were obtained for the numbered actuators (see Figure 5 for the actuator numbering layout for the thin configuration). Profiles through the center of these actuators are shown in Figures 6 and 7.

As can be seen, the influence function depends on the distance of the actuator from the clamped edge of the mirror; the closer to the edge, the more skewed the surface profile.

The mirror surface is measured using a simple, but highly sensitive and accurate technique (see Appendix I for a detailed description). A sinusoidal drive at 500 to 1000 Hz is first applied to the appropriate actuator (or group of actuators). About 30 V rms is used, which produces a peak surface deflection of about 0.079  $\mu\text{m}$ . A phonograph needle is then drawn across the surface and the resulting output is observed on an rms voltmeter as a function of the needle location. The observed profiles are repeatable to within a few percent. This technique is particularly useful because it gives the

---

\*The same mirror was employed in each test. The thick faceplate (0.150 in.) properties were determined with the mirror in an unpolished state. Prior to the polishing and subsequent use of the mirror in the COAT system, it was determined that more favorable operation would result if the faceplate was thinned to 0.125 in. This is the result of a compromise between surface ripple and servo cross coupling, to be discussed below.



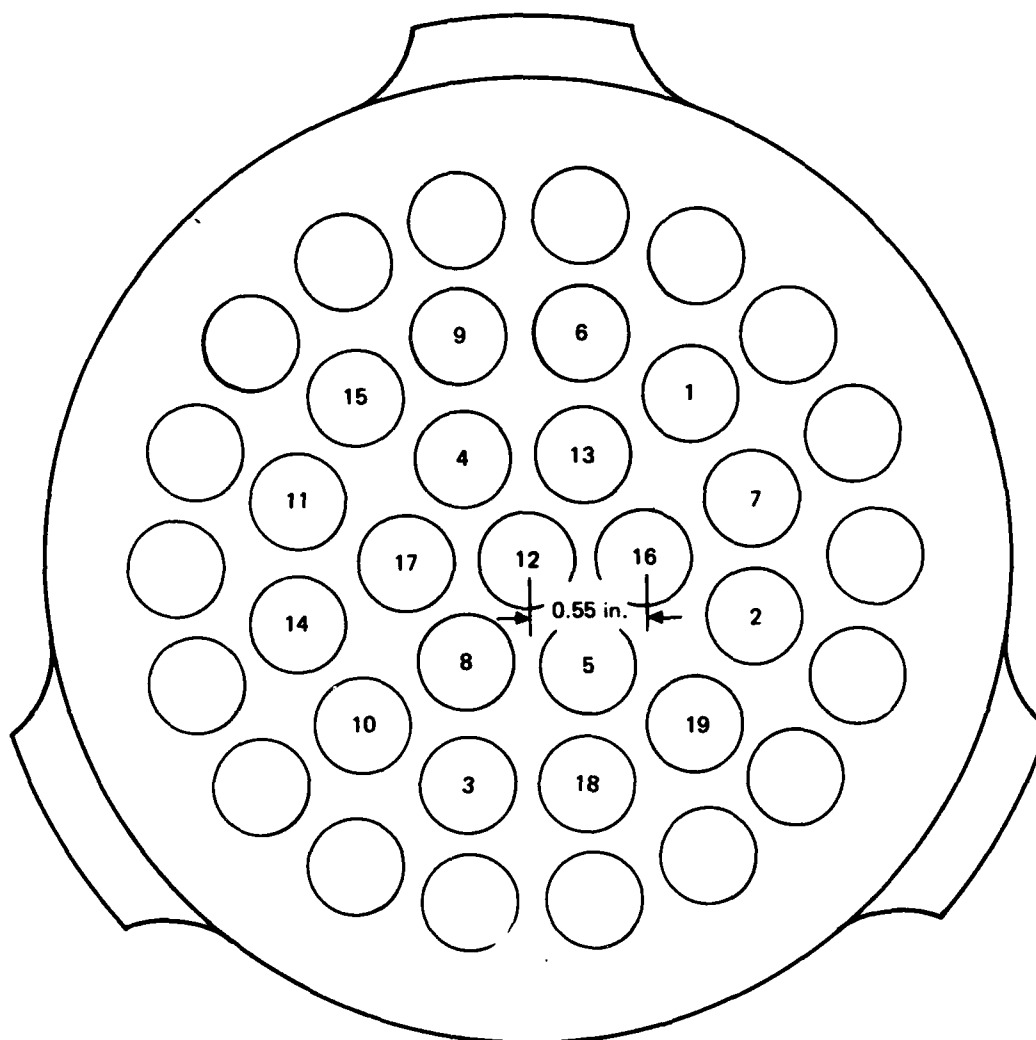
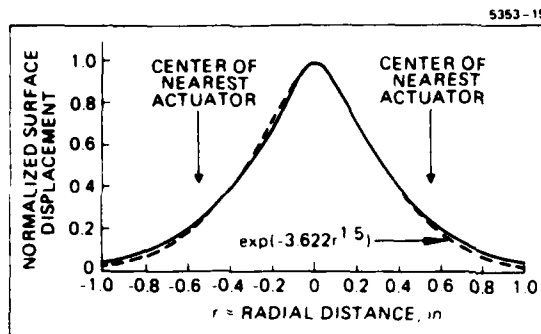
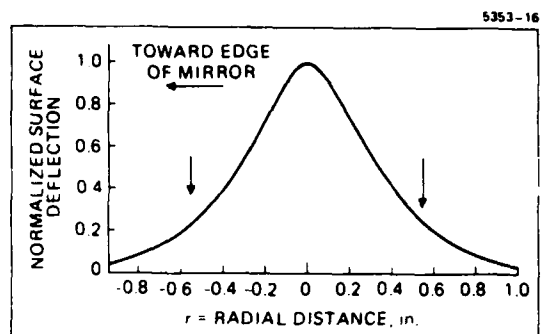


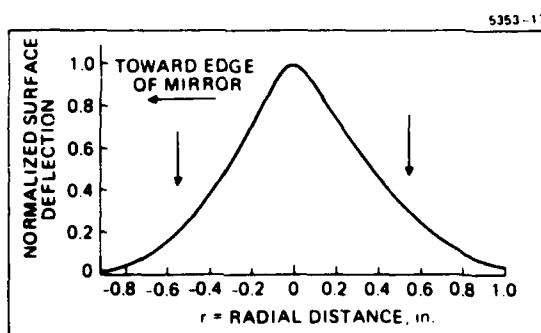
Figure 5. DARPA/RADC actuator location numbering guide.



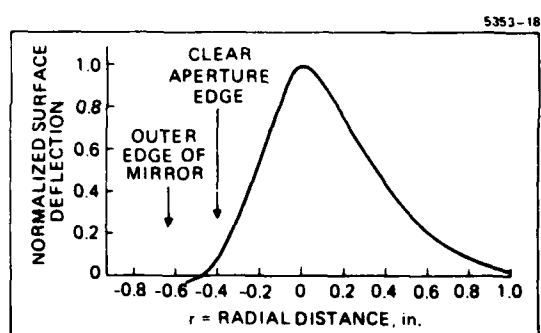
(a)



(b)



(c)



(d)

Figure 6. Influence function profiles of beryllium mirror (0.150 in. thickness). (a) Center actuator. (b) First ring actuator. (c) Second ring actuator. (d) Third (outermost) ring actuator. An empirical curve fit to the central actuator profile is shown as a dotted line in (a); the curve is  $\exp(-3.122 r^{1.5})$ , where  $r$  is the radial distance from the profile peak (actuator center) in inches. The inter-actuator center-center spacing is 0.55 in.

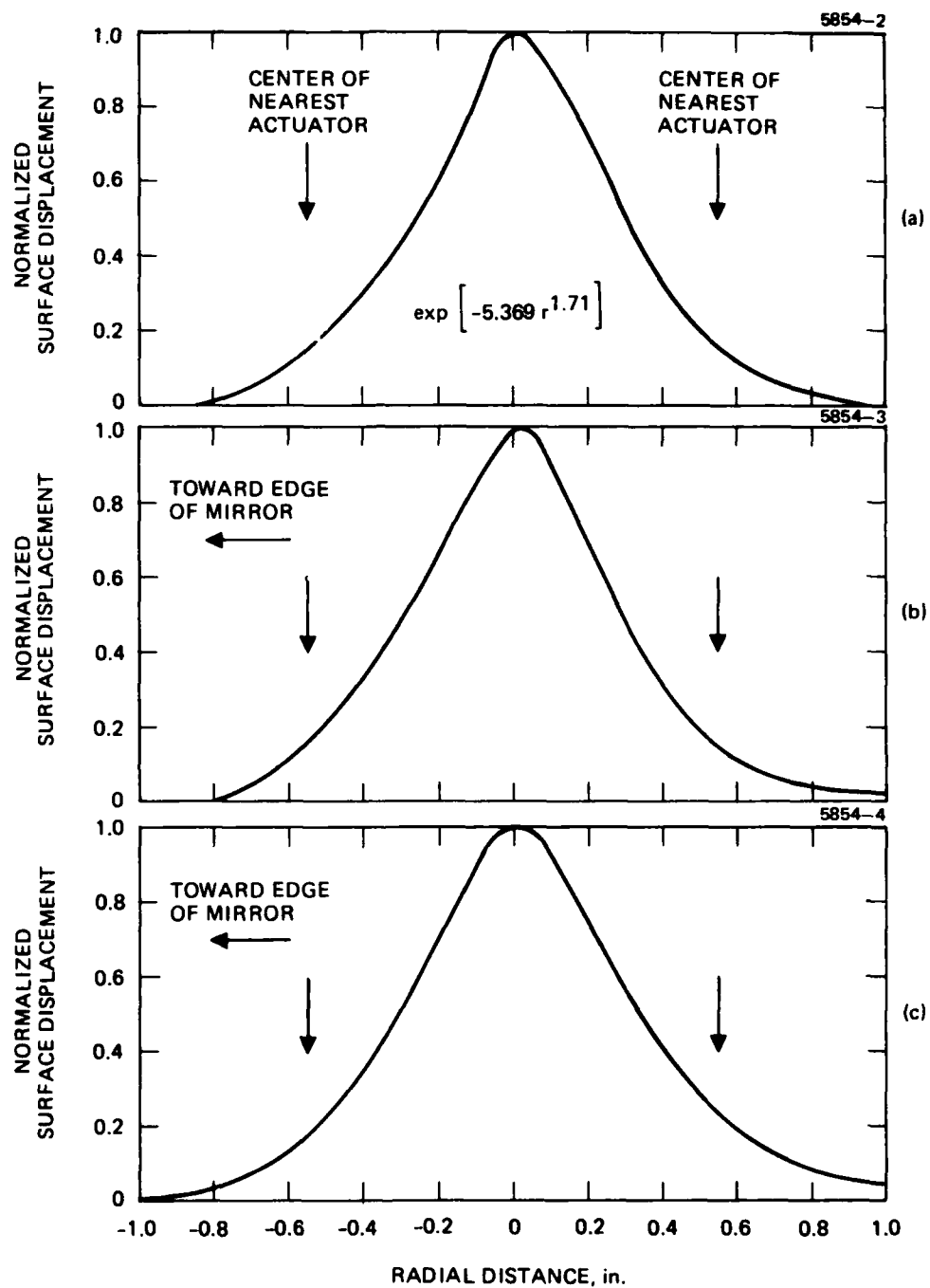


Figure 7. Influence function profile of beryllium mirror (thin faceplate), (a) Center actuator, No. 12. (b) First ring actuator, Nos. 16 or 17. (c) Second ring actuator, No. 1 or 11.

actuator influence function independent of the undriven mirror surface shape. For use on polished mirrors, the needle tip is dipped in epoxy to form a nonabrasive rounded surface. The epoxy produces very little loss in sensitivity.

These measurements were correlated to an analytic model with the aid of the Hughes finite element structure program. The program was exercised with faceplate thicknesses of 0.080 in. and 0.150 in.; the results are plotted in normalized form in Figure 8. Also plotted is the data from central actuator measurements for both the thick and thin faceplates. Correlation is good except in the immediate vicinity of the neighboring actuator. This is primarily due to the unexpectedly high compliance of the actuator stacks.

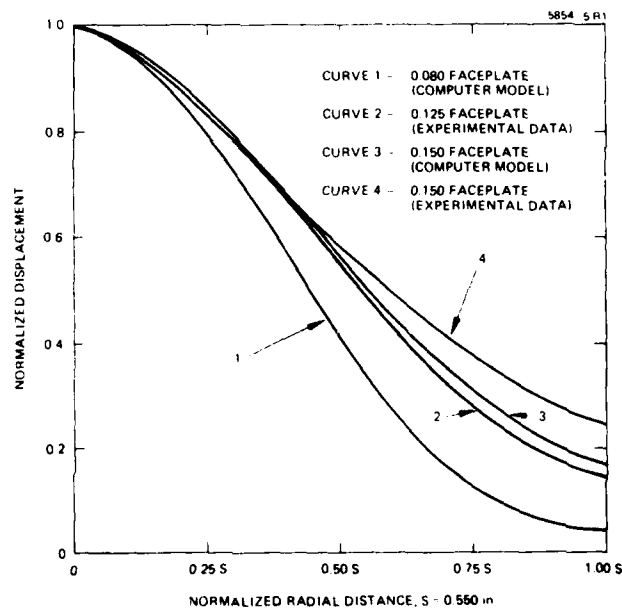


Figure 8. RADC mirror faceplate influence function actuator spacing(s) = 0.550 in.

As indicated in Figure 6(a), the central actuator influence function for the thick faceplate can be approximated by the "subgaussian" function,

$$IN(r) = \exp(-3.622 r^{1.5}) \quad , \quad (6)$$

where  $r$  is the radial distance in inches from the actuator center. Figure 9 shows a 3-dimensional plot of this function and Figure 10 is a contour-line plot of this profile. Notice that the profile is reasonably symmetric, but is slightly higher at the location of the actuator marked (a) than at other actuator locations.

If we define a mechanical coupling,  $C_m$ , as

$$C_m = IN(S) \quad , \quad (7)$$

where  $S$  is the interactuator center-center spacing, then  $C_m = 0.23$  for the thick faceplate mirror. Correspondingly, for the thin faceplate, the influence function can be approximated by  $IN(r) = \exp(-5.369 r^{1.71})$  and  $C_m = 0.15$ .

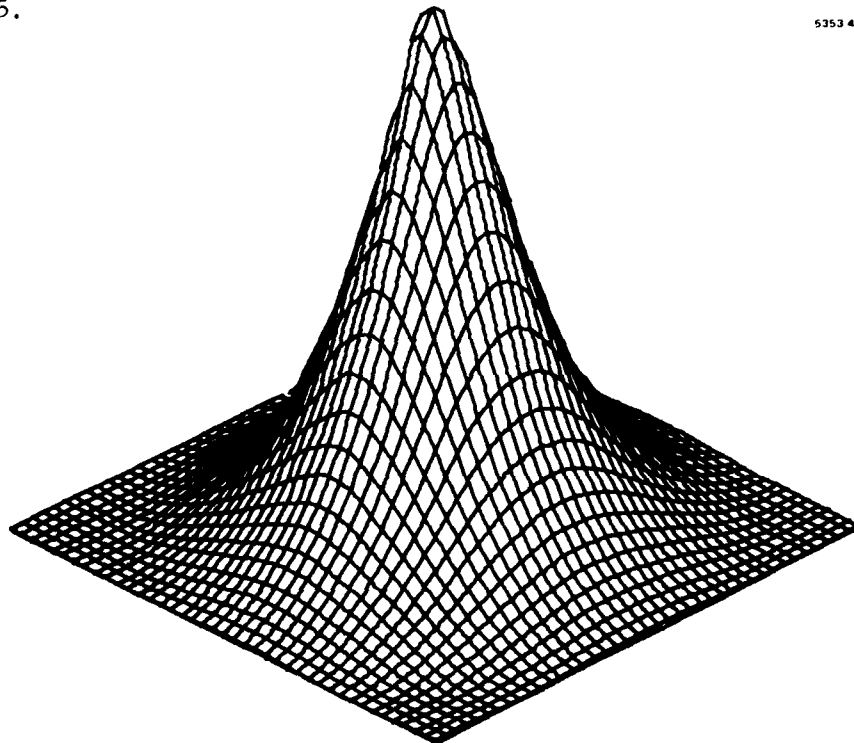


Figure 9. Three-dimensional view of central-actuator influence function for RADC beryllium mirror.

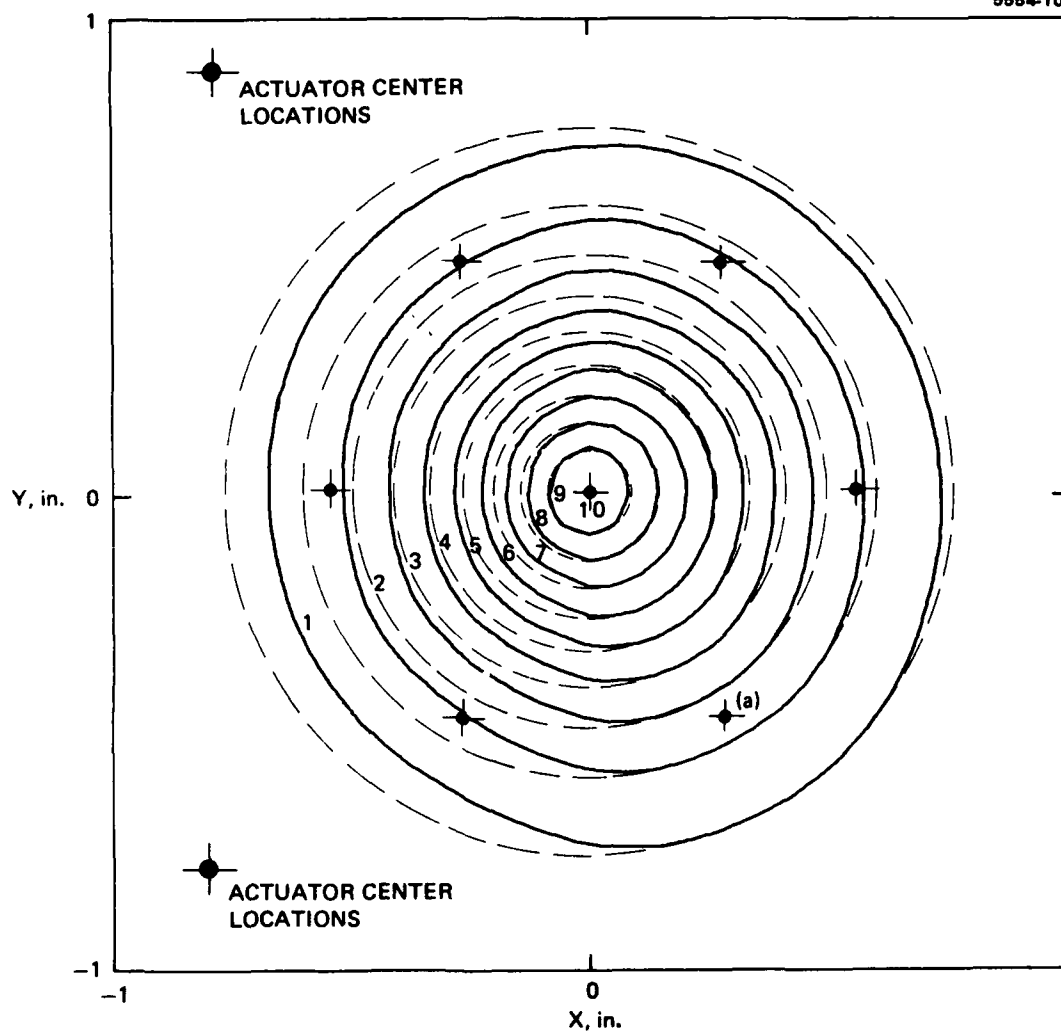


Figure 10. Contour lines of measured profile of center actuator in DARPA/RADC mirror.

### Servo Coupling and Ripple

A more important coupling parameter is the servo coupling,  $C_{sn}$ . O'Meara<sup>2</sup> has defined this coupling as the ratio of the error signal induced in a given channel by the displacement of a single neighboring actuator to that induced by a comparable displacement of the actuator associated with the given channel. When the influence function is of the form

$$IN(r) = \exp \left[ - \left( \frac{r}{r_o} \right)^n \right], \quad (8)$$

where  $r^2 = x^2 + y^2$  is the squared distance from the actuator center, then the servo coupling is

$$C_{sn} = \frac{n 2^{2/n}}{2\pi \Gamma(2/n)} I_n, \quad (9)$$

where  $n$  is any number,  $\Gamma(x)$  is the gamma function, and

$$I_n = \iint \exp \left\{ - \left[ x^2 + y^2 \right]^{n/2} - \left[ (x - \beta)^2 + y^2 \right]^{n/2} \right\} dx dy. \quad (10)$$

The quantity  $\beta$  is given by

$$\beta = \frac{S}{r_o} = (-\ln C_m)^{1/n}. \quad (11)$$

Table 3 and Figure 11 give several values of  $C_{sn}$  for the cases  $n = 1.5, 2.0$ , and  $2.5$  and for 5 values of  $C_m$ . As can be seen, the coupling is significantly larger for the "sub-Gaussian" mirror ( $n = 1.5$ ), but comparable for the Gaussian and "super-Gaussian" ( $n = 2.5$ ) mirrors.

For the RADC mirror with the thick faceplate prior to polish with  $n = 1.5$  and  $C_m = 0.23$ , the servo coupling was  $C_{sn} = 0.7$ . For the thin faceplate version now employed in the COAT system, with  $n = 1.71$  and  $C_m = 0.15$ , we find that  $C_{sn} = 0.42$ .

TABLE 3. SERVO COUPLING COEFFICIENTS

| $\lambda_{opt}$  | 1    | 1.5  | 1.5  | 1.5  | 1.5  | 2    | 2    | 2    | 2    | 2    | 2.5  | 2.5  | 2.5  | 2.5  | 2.5  |
|------------------|------|------|------|------|------|------|------|------|------|------|------|------|------|------|------|
| $\lambda_{opt}$  | 2    | 5    | 10   | 15   | 20   | 2    | 5    | 10   | 15   | 20   | 2    | 5    | 10   | 15   | 20   |
| $C_{sn}$ (eq. 7) | 17.5 | 30.0 | 44.2 | 57.8 | 67.2 | 14.1 | 22.4 | 31.6 | 38.8 | 44.2 | 16.0 | 23.2 | 31.6 | 36.8 | 41.8 |

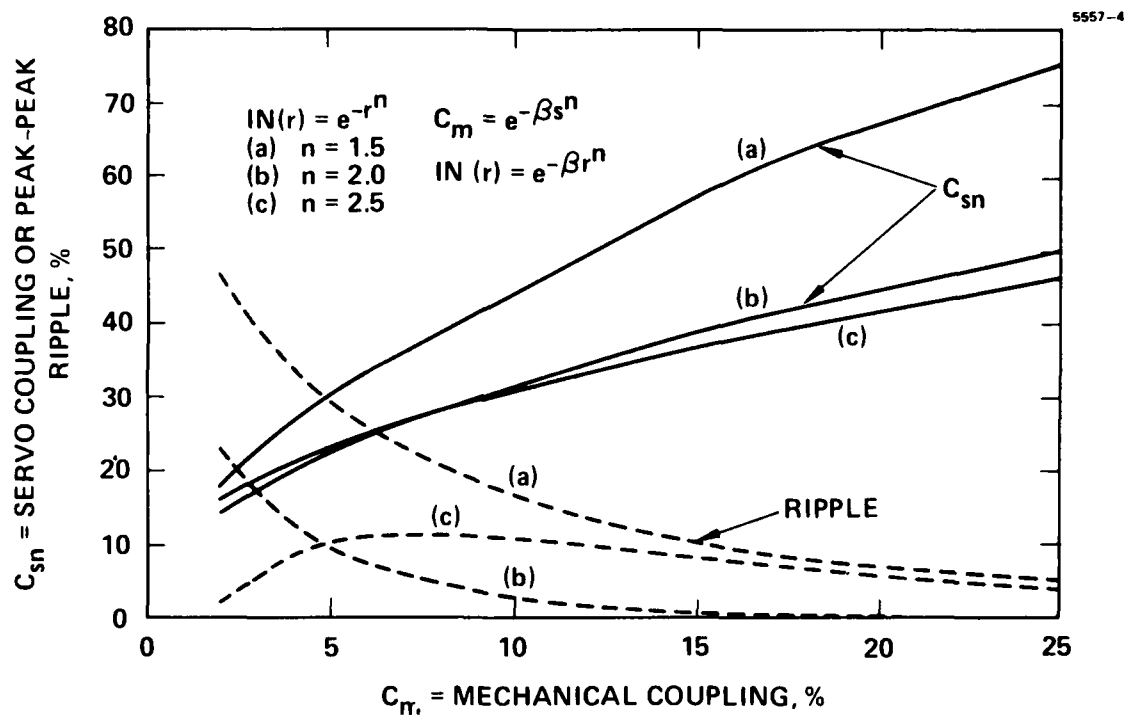


Figure 11. Servo coupling,  $C_{sn}$  (eq. (9)) and peak-peak ripple as a function of deformable mirror mechanical coupling,  $C_m$  (eq. 7)).



The later coupling, while reduced considerably from the 0.7 value, is still large. It is not clear how this will affect the COAT system performance although the results from the system to date (to be described later in this report) indicate the system is operating well.

The only way to reduce the servo coupling once  $n$  is fixed, Eq. (8), is to narrow the influence function, i.e. reduce  $C_m$ . Studies conducted on the Hughes IR&D program, however show that  $n = 2.0$  minimizes  $C_{sn}$  for a fixed value of  $C_m$ . On the other hand, reducing  $C_m$  will increase the inter-actuator ripple (surface ripple when all actuators have equal excitation). The tradeoff between ripple and  $C_{sn}$  as a function of  $C_m$  is shown in Figure 11. (Table 4 gives ripple data.) The ripple data are obtained by calculating the surface produced by a 99-actuator, hexagonal-array mirror. Each actuator is given a unit amplitude deflection and all actuators are assumed to be a linear superposition of all the individual actuator influence functions. This is an approximation, but one which should be reasonably good as long as the actuator restoring springs dominate the inter-actuator surface "springs" caused by the faceplate stiffness (this is expected to be the case in the RADC mirror).

For the particular case of 10% mechanical coupling, a cross-section of the resulting mirror surfaces for the three influence functions for  $n = 2.5$ , 2, and 1.5, are shown in Figure 12a, b, c, respectively. The gaussian mirror has by far the minimum ripple, 2.6%, compared to 16.7% and 10.9% for the subgaussian and supergaussian functions, respectively.

Note in Figure 11 that curves (b) and (c), for the ripple, cross. This implies that, for a given  $C_m$ , there is a value of  $n$  in Eq. (8) that minimizes the ripple. This optimum exponent is plotted in Figure 13 as a function of  $C_m$ . For large  $C_m$ , the value of  $n_{opt}$  approaches 2.0, a gaussian. For all cases, however,  $n_{opt} > 2.0$ , so the RADC mirror is expected to have a larger surface ripple when excited than a mirror with a gaussian influence function.

The experimentally observed surface profile when two adjacent actuators are driven with the same voltage is shown in Figure 14 for the thick faceplate, and Figure 15 for the thin faceplate. Referring to Figure 14, the

TABLE 4. MAXIMUM PEAK-PEAK SURFACE RIPPLE FOR HEXAGONAL ACTUATOR ARRAY, DEFORMABLE MIRRORS

| n   | 1.5  | 1.5  | 1.5  | 1.5  | 1.5 | 2    | 2   | 2   | 2   | 2   | 2.5 | 2.5  | 2.5  | 2.5 | 2.5 |
|---|------|------|------|------|-----|------|-----|-----|-----|-----|-----|------|------|-----|-----|
| $C_M$ , %                                       | 2    | 5    | 10   | 15   | 20  | 2    | 5   | 10  | 15  | 20  | 2   | 5    | 10   | 15  | 20  |
| Peak-peak ripple, percent of maximum deflection | 46.5 | 29.2 | 16.7 | 10.6 | 7.1 | 22.9 | 9.2 | 2.6 | 0.8 | 0.2 | 2.0 | 10.4 | 10.9 | 8.5 | 5.5 |

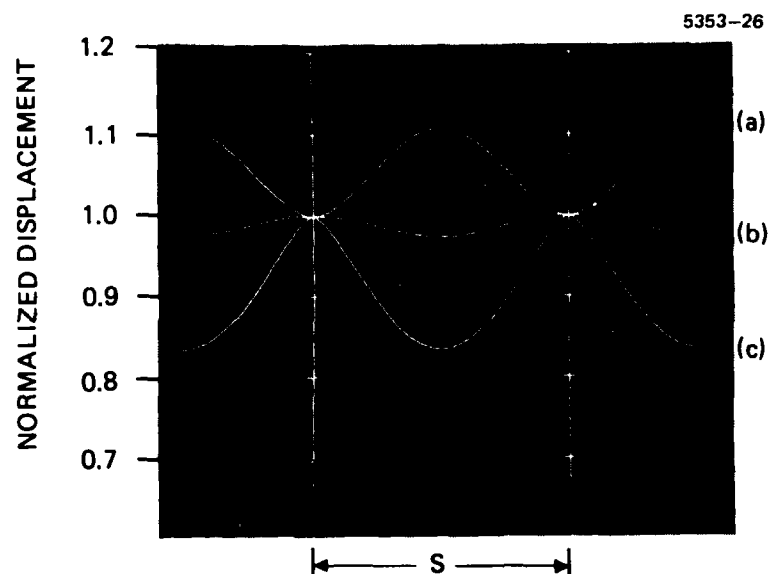


Figure 12. Cross-sectional profiles of deformable mirror for three influence functions.

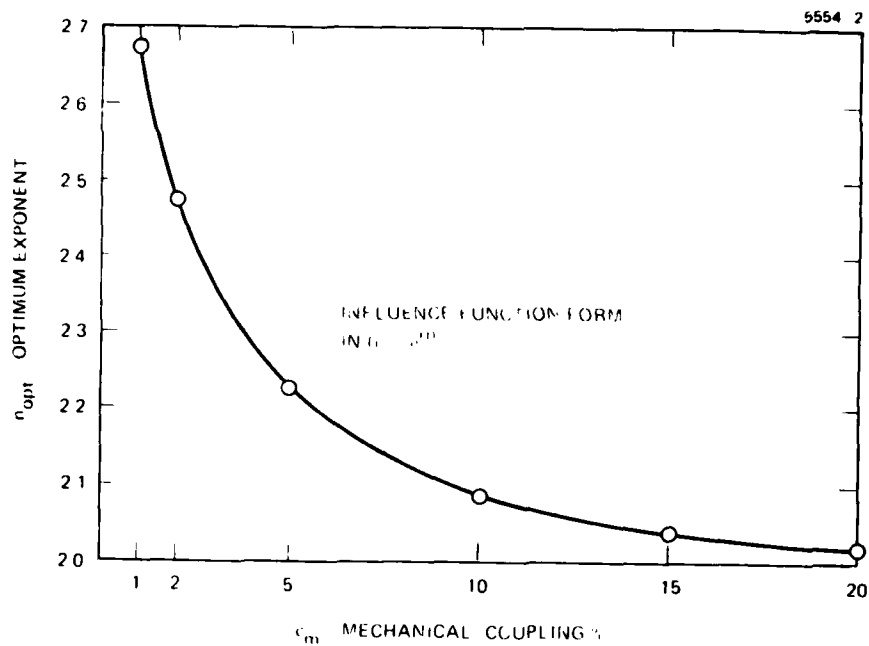


Figure 13. Optimum value of exponent,  $n$ , in eq. (3) in order to produce minimum surface ripple.

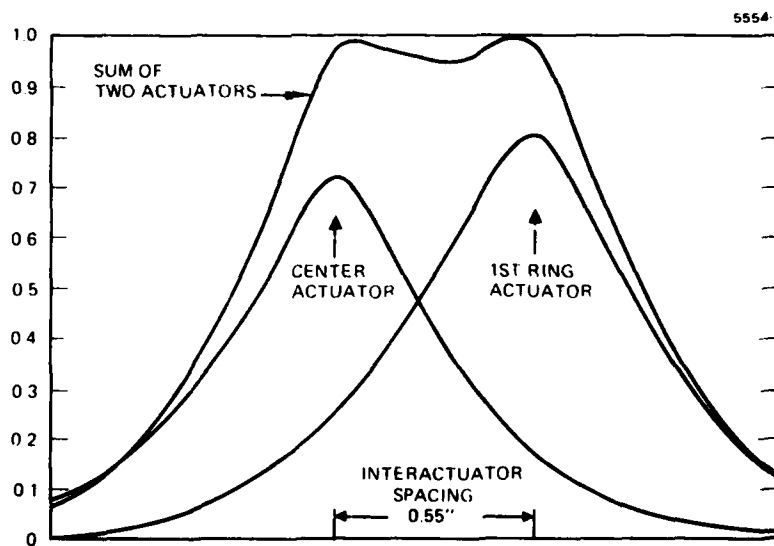


Figure 14. Experimentally observed surface profile with two adjacent actuators on DARPA/RADC mirror driven with equal voltage ( $\sim 30$  V rms at 500 Hz). The individual actuator influence functions that produce the resultant surface are also shown.

peak-to-peak surface ripple is 4.9% of the surface deflection at one actuator location. Figure 11 predicts 8% ripple if all actuators are energized. A simple superposition of two actuators with the same influence function,  $IN = \exp \left[ - (r/r_o)^{1.5} \right]$ , and 23% coupling, predicts a 3.3% ripple. The difference between this value and the observed 4.9% can be attributed to the differences between the two influence functions in Figure 14; they are not identical.

Referring to Figure 15, for the thin faceplate the peak-to-peak surface ripple is 15% at one actuator location. A simple superposition gives 12% ripple.

Based on these results for servo coupling and mirror ripple, it appears that a nearly gaussian influence function is a desirable characteristic for a deformable mirror, and that a mechanical coupling coefficient of between 10% and 15% is a reasonable compromise between minimum ripple and servo channel cross coupling.

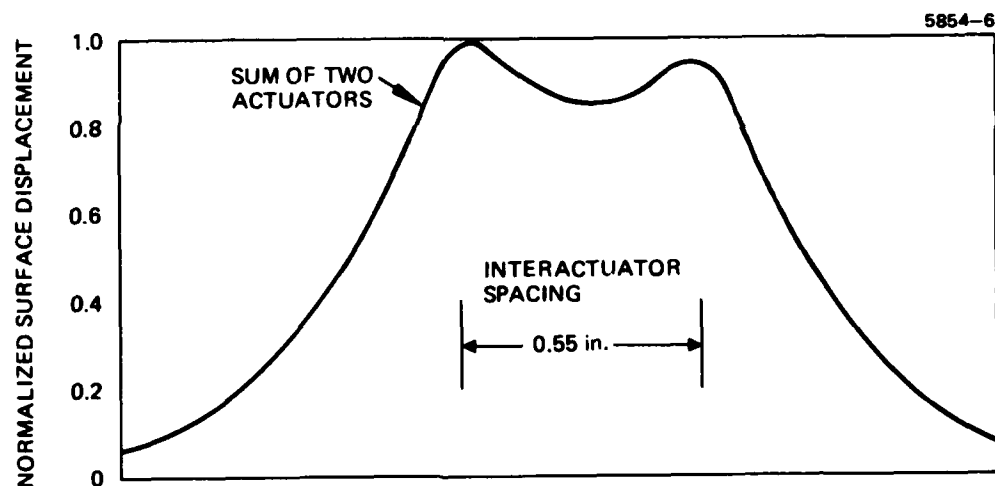


Figure 15. Experimentally observed surface profile with two adjacent actuators on beryllium mirror driven with equal voltage. Actuator No. 12 and 17 driven.

## DISPLACEMENT SENSITIVITY

### Static Performance — Single Actuator Motion

Theoretical Predictions. The surface motion of an actuator is heavily influenced by the degree of cross-coupling to neighboring actuators. The mirror and its actuator stacks were originally designed for a relatively low-level cross-coupling factor of about 5%, but the faceplate thickness was increased from 0.060 in. to 0.150 in. to raise the cross coupling to about 23%. This had the net effect of reducing the theoretically available motion of a single actuator from about  $\pm 19.5 \mu\text{in.}$  at  $\pm 150 \text{ V}$  to about  $11.2 \mu\text{in.}$

In practice, actuator stack assemblies do not produce the total free expansion as expected, typically being limited to about 85%. This translates directly into a 15% reduction in surface motion so that a realistic limit is  $16.6 \mu\text{in.}$  and  $8.24 \mu\text{in.}$ , respectively. Prior to polish, the faceplate thickness was reduced to 0.125 in. as discussed before, to lower the cross-coupling factor to about 15%. The predicted response for a single actuator is  $\pm 10.4 \mu\text{in.}$  ( $\pm 0.264 \mu\text{m}$ ) at  $\pm 150 \text{ V}$ .

Experimental Measurements. The surface motion was measured using several techniques: (1) As discussed previously using the phonograph needle scheme which gives relative measures of surface motion (see Appendix I); (2) using interferometric techniques to determine absolute surface deflections of single actuators or sets of actuators; and (3) as a check, using a two-hole mask on the mirror which allows only two widely spaced actuators at a time to be illuminated, resulting in an interference pattern. When one actuator is then energized the fringe pattern is caused to shift an amount dependent upon the peak surface motion of that actuator.

The relative peak surface deflection using method (1) is shown in Table 5. There is a variation in relative deflection, from a maximum for actuator No. 16 to the minimum for actuator No. 3, of a factor of 3. The results from method (3) gave virtual agreement with these relative values.

The absolute surface deflection was determined from method (2). For actuator No. 16 the interferogram result is shown in Figure 16 with +150 V applied to the actuator. Also shown in Figure 16 is a reference

TABLE 5. ACTUATOR PEAK SURFACE DEFLECTION

| Actuator Number | Normalized Deflection |
|-----------------|-----------------------|
| 1               | 0.343                 |
| 2               | 0.577                 |
| 3               | 0.319                 |
| 4               | 0.388                 |
| 5               | 0.585                 |
| 6               | 0.411                 |
| 7               | 0.418                 |
| 8               | 0.421                 |
| 9               | 0.475                 |
| 10              | 0.714                 |
| 11              | 0.623                 |
| 12              | 0.479                 |
| 13              | 0.498                 |
| 14              | 0.621                 |
| 15              | 0.545                 |
| 16              | 1.00                  |
| 17              | 0.437                 |
| 18              | 0.349                 |
| 19              | 0.331                 |

interferogram at zero voltage. From these interferograms we can estimate an absolute deflection of  $\pm 0.47 \mu\text{m}$  for  $\pm 150 \text{ V}$ . Thus for actuator No. 3 the absolute deflection is  $\sim \pm 0.15 \mu\text{m}$  for  $\pm 150 \text{ V}$ . Using Table 5 we determine that on the average the actuator surface motion is  $\pm 0.2 \mu\text{m}$  for  $\pm 150 \text{ V}$ . This is reasonably close to the theoretically predicted value of  $\pm 0.264 \mu\text{m}$ . The wide variation in surface motion between the various actuators is most likely due to unaccounted-for compliance in the actuator stack assembly. Past experience has shown that such compliance occurs for several reasons, primarily: (1) Poor seating on the end caps resulting in point contact loading, (2) excessive warping of piezoelectric washers in stack, and (3) excessive soft material such as epoxy or solder between washers in the stack. Identification of the source of compliance may lead to further improvement of mirror motion characteristics.

#### Static Performance — Gross Surface Motion

The gross surface motion of the mirror is the upper bound of travel of the mirror surface when all actuators are driven to the maximum voltage. In this manner, faceplate cross-coupling is eliminated except at the brazed outer periphery. Theoretically, the gross surface motion should be  $\pm 21.0 \mu\text{in.}$  ( $0.53 \mu\text{m}$ ) at  $\pm 150 \text{ V}$  (including the 15% reduction). This figure represents the design goal for the faceplate excursion discussed in Table 1 earlier.

Interferograms have been taken with all the actuators energized to  $+150 \text{ V}$ ; Figure 17 is typical of the results obtained. It is difficult to observe the expected factor-of-two increase in surface motion with all actuators energized relative to one actuator energized (Figure 16). This is complicated by three factors: first, the periphery of the mirror holds the surface and prevents the larger fringe shifts from being observed; second, due to the large fringe shift of actuator No. 16 relative to surrounding ones (factor of 3 greater) it is difficult to see the other motions; and third, due to the wide variation of individual actuator motion, factor-of-two increase in fringe shift from a base of only  $\sim 1/3$  fringe shift is difficult to see. However, we see from Figure 17 that motion is observed in a direction consistent with increased deflection relative to Figure 16.\*

\*Later work on other deformable mirrors of larger diameter has shown quantitatively the factor-of-two increase.

5854-7



REFERENCE  
ZERO VOLTAGE

(a)

5854-8



+ 150 V

(b)

Figure 16. Interferogram of actuator No. 16.



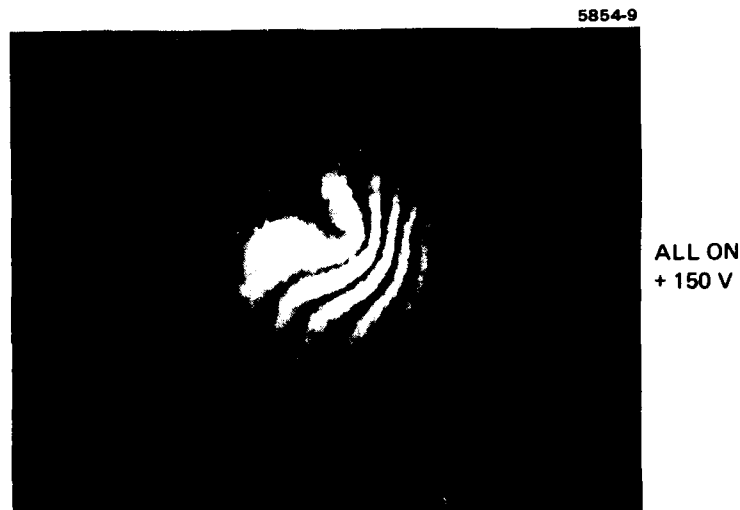


Figure 17. Interferogram of all actuators on +150 V.

In addition to surface motion measurements local slope measurements were made by driving adjacent actuators at +150 V and -150 V. The results indicated that the surface could be deflected at this condition and achieve full displacement with no stress problems.

#### Dynamic Performance

The structural complexity of deformable mirrors does not lend itself to a direct all encompassing analysis of the dynamic characteristics. Instead, methods for examining different classes of modal response have been developed. These are: actuator resonance modes; backup structure resonance modes, and faceplate resonance modes.

Actuator modes are easiest to analyze since they are well characterized by two natural frequencies. The actuator modes have calculated natural frequencies of 40.5 kHz and 67.1 kHz.

Backup structure modes are more complex and must be determined by use of finite element structural models. The first four natural frequencies were determined to be 13 kHz, 18.2 kHz, 21.6 kHz and 26.5 kHz.

Faceplate modes are by far the most difficult to assess and have not as yet been analyzed in detail. Order of magnitude estimates indicate that faceplate natural frequencies occur no lower than about 40 kHz.

Analytic techniques for studying dynamic interaction between the various classes of vibrational modes have not as yet been developed. In spite of this, correlation between analytic and experimental results has been good. The frequency response curve taken on the center actuator (Figure 18) indicates low-level resonances in the 12 to 15 kHz range, the 18 to 20 kHz range, and at about 24 kHz. Since there are only small variations in the phase lag in these regions, this activity is due to excitation of backup structure modes. Since more complex behavior occurs in the region above 24 kHz, it is more difficult to discern the exact nature of the behavior. The large drop in phase lag in the 40 to 50 kHz band is indicative of an actuator-type resonance. Also, since the response does not roll off immediately above this region, it must be concluded that the second actuator natural frequency is about 50 kHz. This behavior is consistent with the analytical results.

In addition to this data for the central actuator resonance, data was taken at actuators on the first and second rings. The prominent resonant frequencies with their relative amplitudes are given in Table 6 for selected actuators on these rings. This data follows the above trends consistently.

It has been demonstrated on other deformable mirrors that oil damping of the faceplate has a dramatic effect on the frequency response. The primary effect is to damp faceplate and actuator resonances and to smooth the phase-lag characteristic. The result is a smooth, regularized response plot that clearly shows the actuator resonances in a low-Q profile, and eliminates sharp variations in the phase-lag plot. Based on experience with other mirrors, damping can potentially increase the usable bandwidth to the vicinity of the second actuator resonance (67.1 kHz).

### Hysteresis

The piezoelectric ceramic material used in the RADC mirror is of the "soft" variety. It has a relatively low Young's modulus but a high piezoelectric charge coefficient, also known as the  $d_{33}$  constant. Hysteresis loops using this material can be larger than those exhibited with the "hard," low  $d_{33}$  materials.

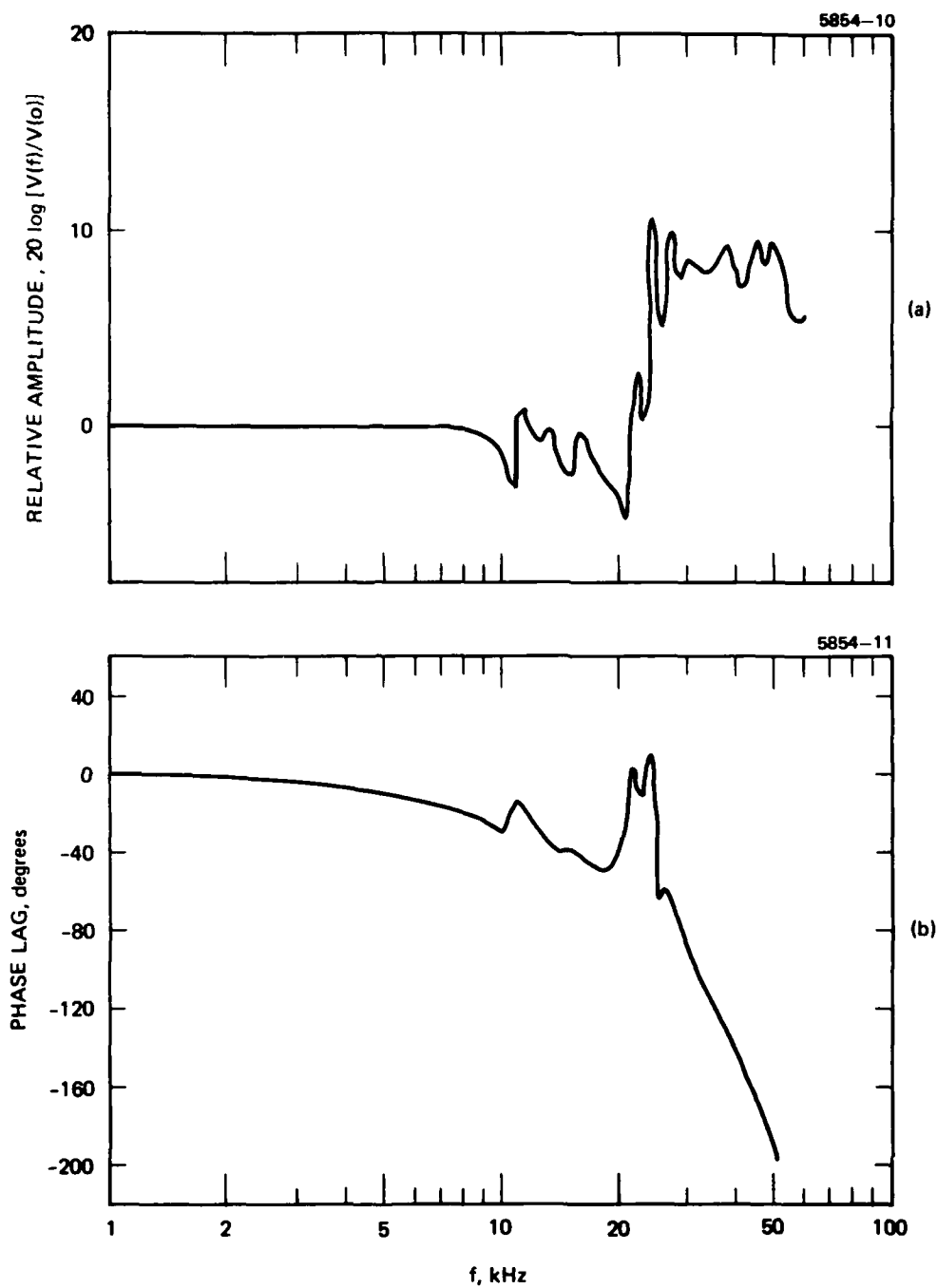


Figure 18. Amplitude (a) and phase (b) response for central actuator of beryllium mirror. Faceplate thickness 0.125 in. Drive to actuator is 100 V peak-peak, producing  $0.1 \mu\text{m}$  faceplate motion.

TABLE 6. PROMINENT RESONANCE FREQUENCIES

| f, kHz                 | Relative Amplitude |
|------------------------|--------------------|
| Actuator No 12, Center |                    |
| 11.5                   | 0.92               |
| 24.5                   | 10.6               |
| 27.3                   | 9.8                |
| No. 17, First Ring     |                    |
| 12                     | 8.8                |
| 21.75                  | 14.8               |
| 28.5                   | 12.7               |
| No. 7 Second Ring      |                    |
| 12                     | 3.3                |
| 24.3                   | 9.5                |
| 31.5                   | 10                 |

Hysteresis is largely a function of electric field in the actuator stack disc elements. When the electrical field is limited to relatively low levels, hysteresis is reduced correspondingly. The RADC stacks were designed to operate at about one-sixth of the depolarizing field strength. The hysteresis loop of the stacks mounted for free expansion were measured to be about 3% to 5% at full drive voltage. Hysteresis measurements made on the mirror after assembly are shown in Figure 19. From the data the hysteresis is less than 1%.

#### Electrical Performance

The electrical capacitance of the stacks was calculated to be about 25,000  $\mu\text{f}$ . Actual measurements showed that stack capacitance varied between 20,000  $\mu\text{f}$  and 26,000  $\mu\text{f}$ . This degree of variation is consistent with past experience, but we believe that greater control during fabrication can result in tighter tolerance of stack capacitance.

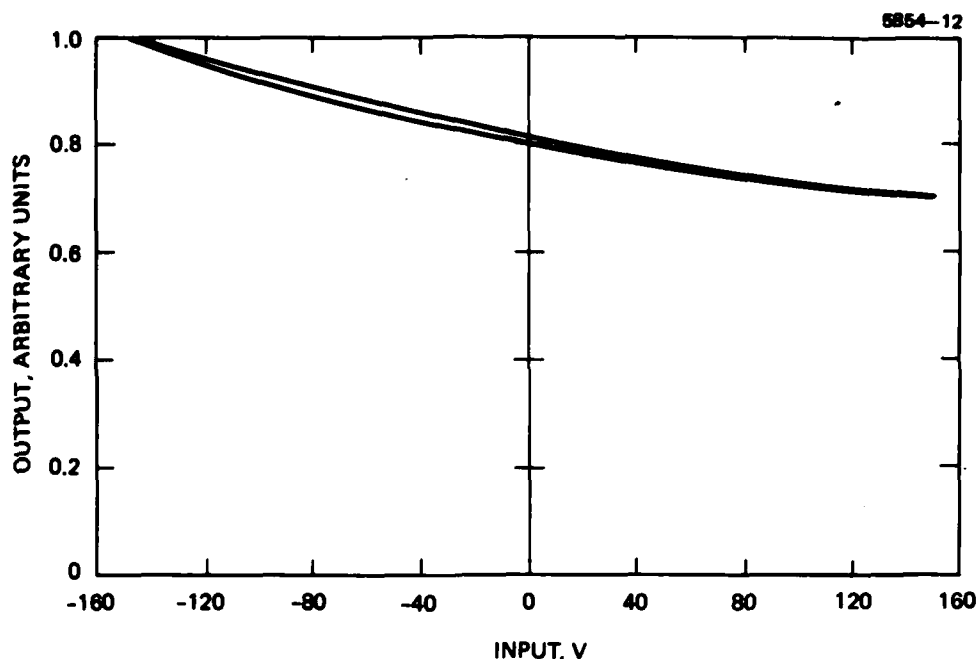


Figure 19. Hysteresis plot for thin faceplate RADC mirror.

The loss tangent was measured to be in the range of 0.015 to 0.020. The loss tangent can be reduced significantly by using the hard ceramic materials. Typically, these materials have loss tangents of 0.005.

#### SURFACE POLISH AND FIGURE

Final optical figure was achieved on the deformable substrate by employing grinding and polishing techniques which were quite similar to those used on other metal mirrors. However, some modifications to the standard procedures were necessitated for polishing the beryllium surface. The toxicity of the beryllium required that care be taken to avoid personnel contamination from the beryllium particles removed during the grinding and polishing. This was controlled by carefully collecting the abrasive slurries utilized during these operations and disposing of them in sealed plastic bags. Although the material used to fabricate the faceplate was an optical grade beryllium, it was found to be highly susceptible to pitting during grinding operations. This

pitting was alleviated by the use of lower tool pressures on the mirror surface. Deionized water was used as the solvent during both grinding and polishing. The reduced tool pressure resulted in a slower material removal rate than that achieved on molybdenum optics of a similar size. Final optical flatness of the surface after polishing is shown in Figure 20. This photo shows the interference pattern for the surface as referenced to a flat test plate. The test wavelength is  $5900 \text{ \AA}$ . The surface is flat within the active aperture to less than  $1/4$  fringe ( $1/8 \lambda$ ). Final surface roughness was approximately  $75 \text{ \AA}$  rms.

The above data is for the mirror before use in the COAT system. After the mirror had been used, the surface flatness was determined, and the results can be seen from the data of Figure 16(a). It is apparent that no obvious permanent stresses or deformations have occurred.



Figure 20. Optical surface figure after polishing.

## ACTUATOR PROPERTIES - DESIGN FORCE AND VOLTAGE

The actuators are designed to produce single-actuator motion against the combined spring loading of the actuator preload mechanism and faceplate. Since the original mirror design incorporated a cross-coupling coefficient of about 0.05, the working spring load was only about half that which the mirror had with a cross-coupling factor of 0.23. Thus, the single-actuator motion was approximately halved. Presently, the mirror has a cross-coupling coefficient of about 0.15. The spring load on a single actuator stack for this condition is  $1.65 \times 10^6$  lb/in. For a  $0.50 \mu\text{m}$  deflection, the force generated would be 32.5 lb. The stress in the actuator stack due to this kind of loading is on the order of 2500 psi (including preload), well within the material stress limits.

The electric field strength was designed to be about one-sixth of the depolarizing field strength, primarily to limit hysteresis effects. An increase of drive voltage to 150 V or 200 V would be permissible electrically, but hysteresis loops would enlarge and the stress limits of the piezoelectric ceramics would be approached.

## FACEPLATE DESIGN CONSIDERATIONS

### Static Stress Limits

The ultimate tensile strength of beryllium is typically 35,000 lb/in.<sup>2</sup> and the yield strength is about 25,000 lb/in.<sup>2</sup>. As a design parameter, the 25,000 lb/in.<sup>2</sup> figure was chosen as the basis of comparison for margin of safety (Eq. (12)) for performance considerations. Since ultimate strength limits are higher, a positive margin of safety on performance is also satisfactory for structural integrity.

$$\text{margin of safety} = \frac{\sigma_{\text{yield}}}{\sigma_{\text{max}}} - 1 \quad (12)$$

The maximum stress occurring in the faceplate is at the outer actuator ring, adjacent to the brazed periphery. This region is under significant bending

stress due to actuator preload and at maximum excursion. The maximum stress in this region is about 20,500 lb/in.<sup>2</sup>, so the margin of safety is 0.22. All other stresses are less than 12,000 lb/in.<sup>2</sup>

The stress incurred in the structure due to maximum local surface slope conditions (30 μin., actuator to actuator) is about 11,000 lb/in.<sup>2</sup>

#### Dynamic Stress Limits

Alternating stresses due to phase correction are about 7350 lb/in.<sup>2</sup> for a maximum 0.50 μm actuator-to-actuator displacement. If the endurance limit is taken as one-half the yield stress, 12,500 lb/in.<sup>2</sup>, the margin of safety (Eq. (13)) is 0.701.

$$\text{margin of safety} = \frac{\sigma_{\text{endurance}}}{\sigma_{\text{max}}} - 1 \quad (13)$$

The stresses due to operation in the multidither mode are even less severe. A 0.05 μm dither stroke per actuator results in up to 0.10 μm interactuator deflection which causes a maximum stress of 1450 lb/in.<sup>2</sup> with a margin of of safety of 7.63.



## DEFORMABLE MIRROR COAT SYSTEM CHARACTERISTICS

### SERVO SYSTEM DESCRIPTION

#### Common Channel Controls

A block diagram of the complete COAT system is shown in Figure 21. In its present configuration 19 actuators are active in the deformable mirror, hence there are 19 servo electronics channels controlling the mirror. After two additional tracking controls and one additional spherical-focus control channel are in operation as shown. The servo control channels for these additional functions were built by dividing the dither frequencies of the 19-channel system by 10 for the tracking channels and by 100 for the focus control.

The functional block diagram of the servo system for the deformable mirror is shown in Figure 22. The receiver is a single photomultiplier and the signal conditioning consists of a preamp, an AGC, a phase reversal switch, a clipper, and a loop gain adjustment. A loop break switch is also provided for "COAT OFF" operation. The available controls on each channel as shown in Figure 22(b) include various monitor and input points distributed throughout the five low-pass filter stages. A photograph of the all-solid-state electronics, including power supplies and AGC networks, is shown in Figure 23. Figure 24 is a photograph of three two-channel control modules which fit in a standard 19-in. wide rack panel. Figure 25 is a photograph of the focus and tracking controls. Figure 26 is a schematic of the focus actuator.

Since the RADCOAT system was built as a research tool and not as an operational prototype for a practical COAT system, a great deal of flexibility and versatility is included in the electronics as well as the optics. The capability for selecting three operating modes for the dither frequencies is possible: One frequency per channel; two channels for each frequency (sine/cosine); and three channels per frequency (triphase). The phase of each dither frequency can also be adjusted independently. Only the first mode of operation has been experimentally studied in detail, using the

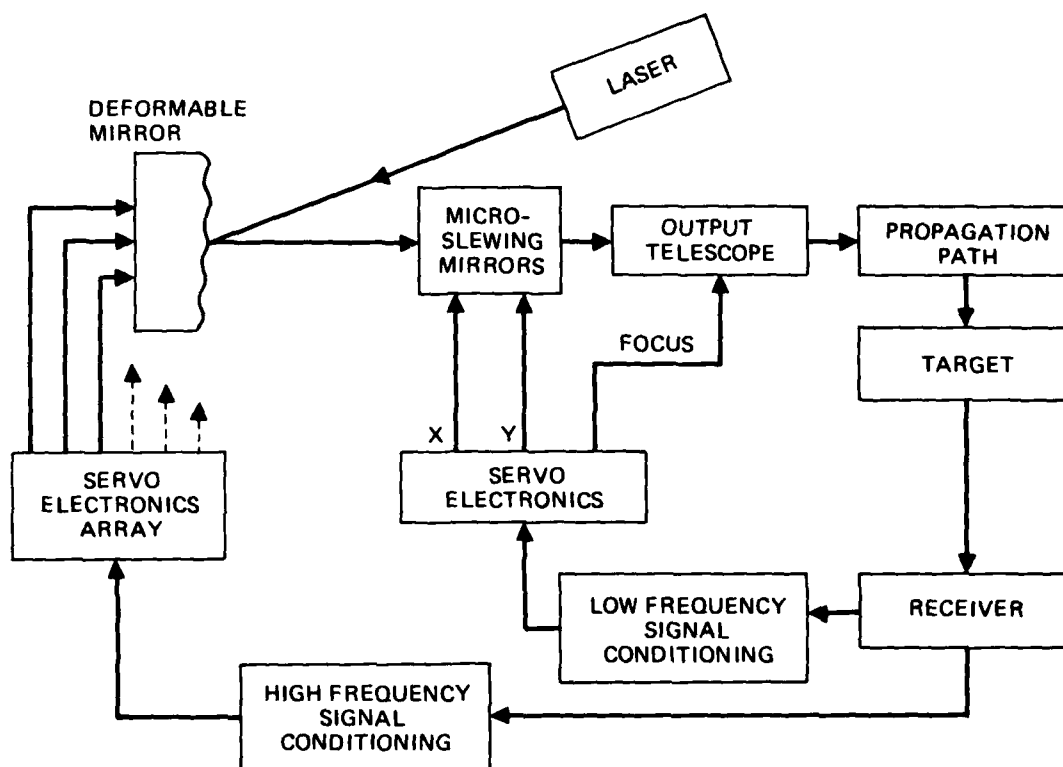


Figure 21. COAT system block diagram showing additional multidither servo loops for tracking and focus control.

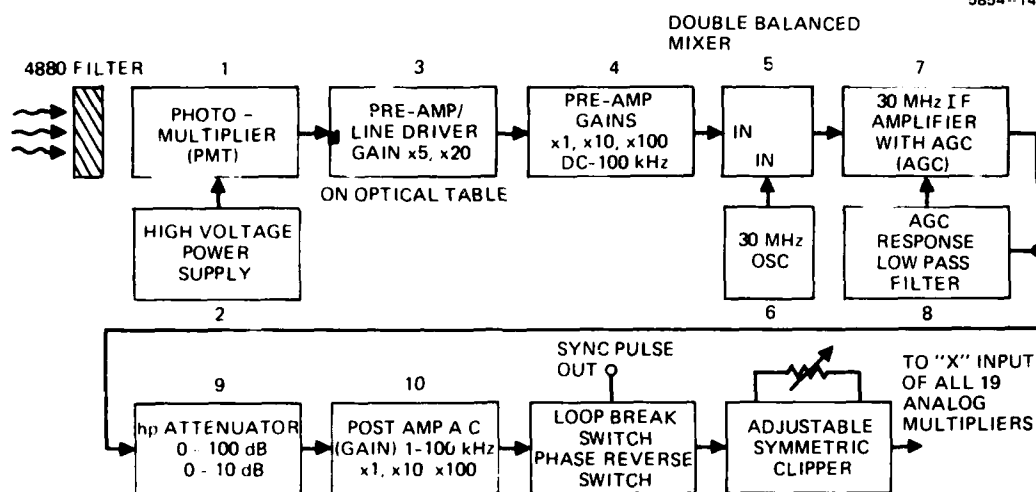


Figure 22(a). Signal conditioning electronics.

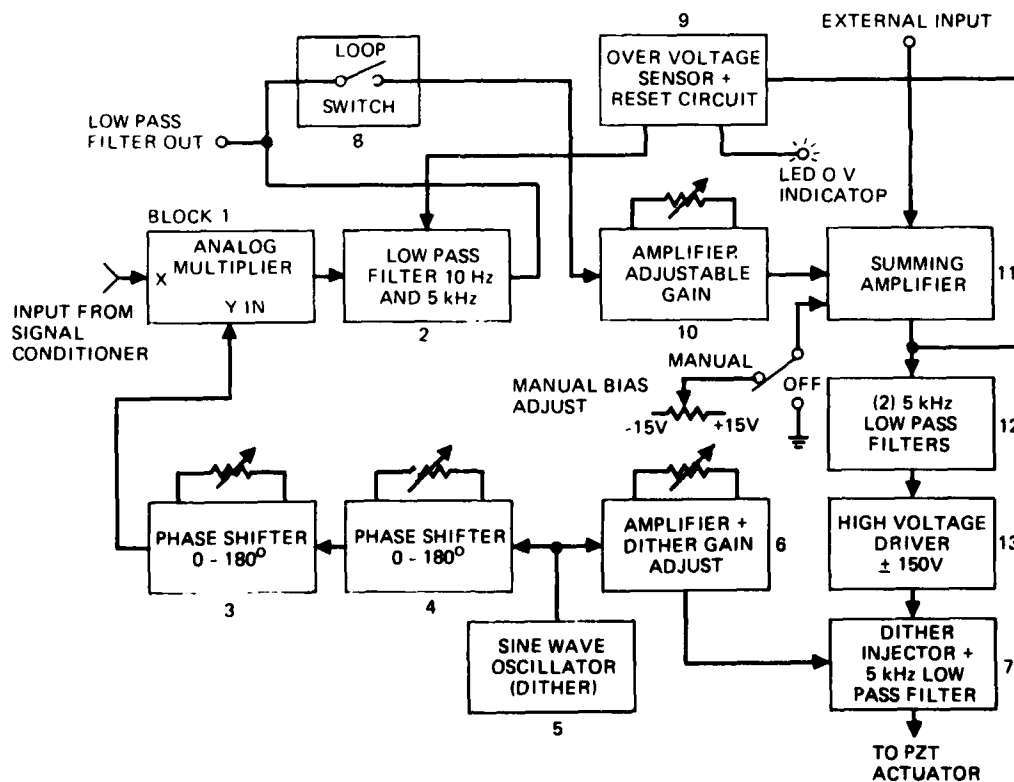


Figure 22(b). COAT servo electronics (one channel shown).

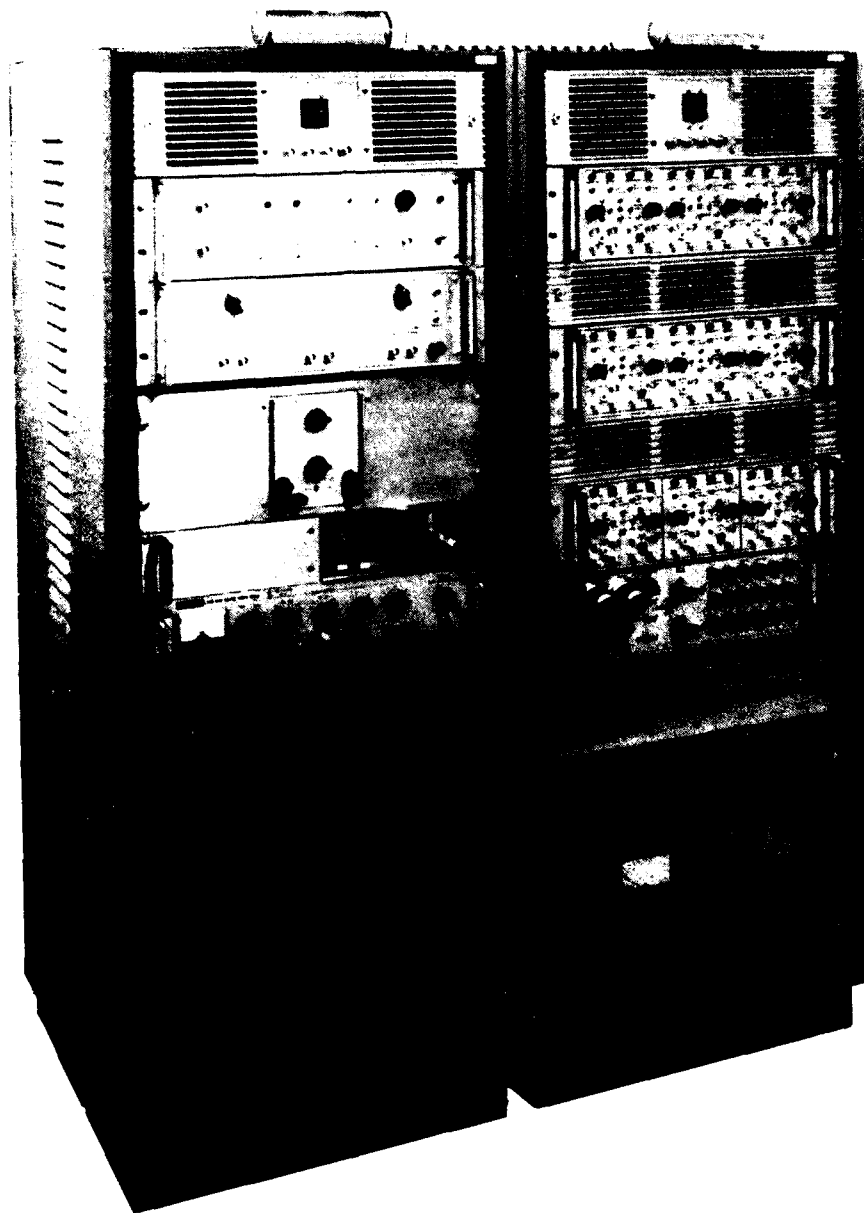


Figure 23. Photograph of complete RADC/COAT control electronics.

M9937

3489-105

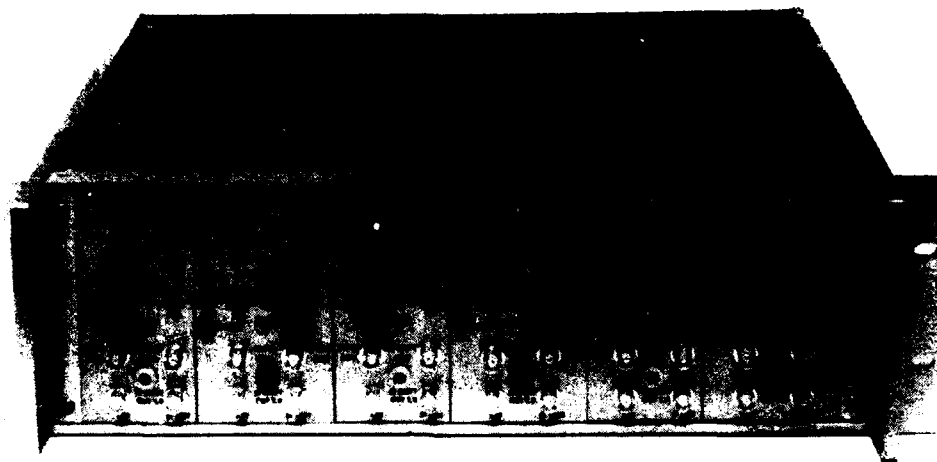


Figure 24. Photograph of a 6-channel COAT electronics panel.

M10929

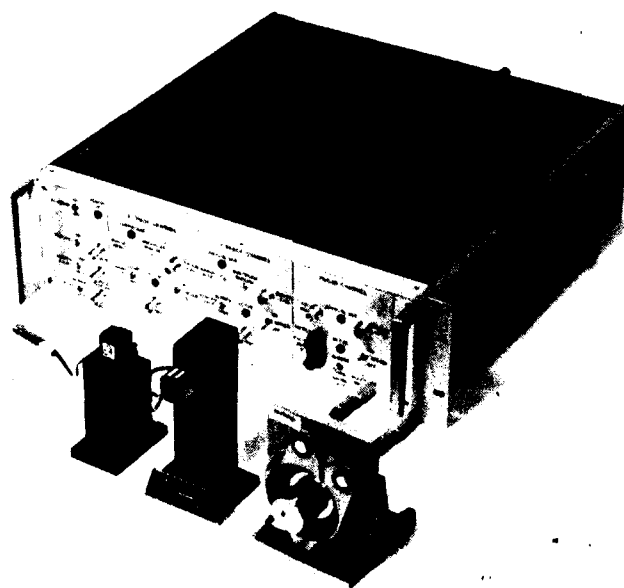


Figure 25. Focus and tracking controls.

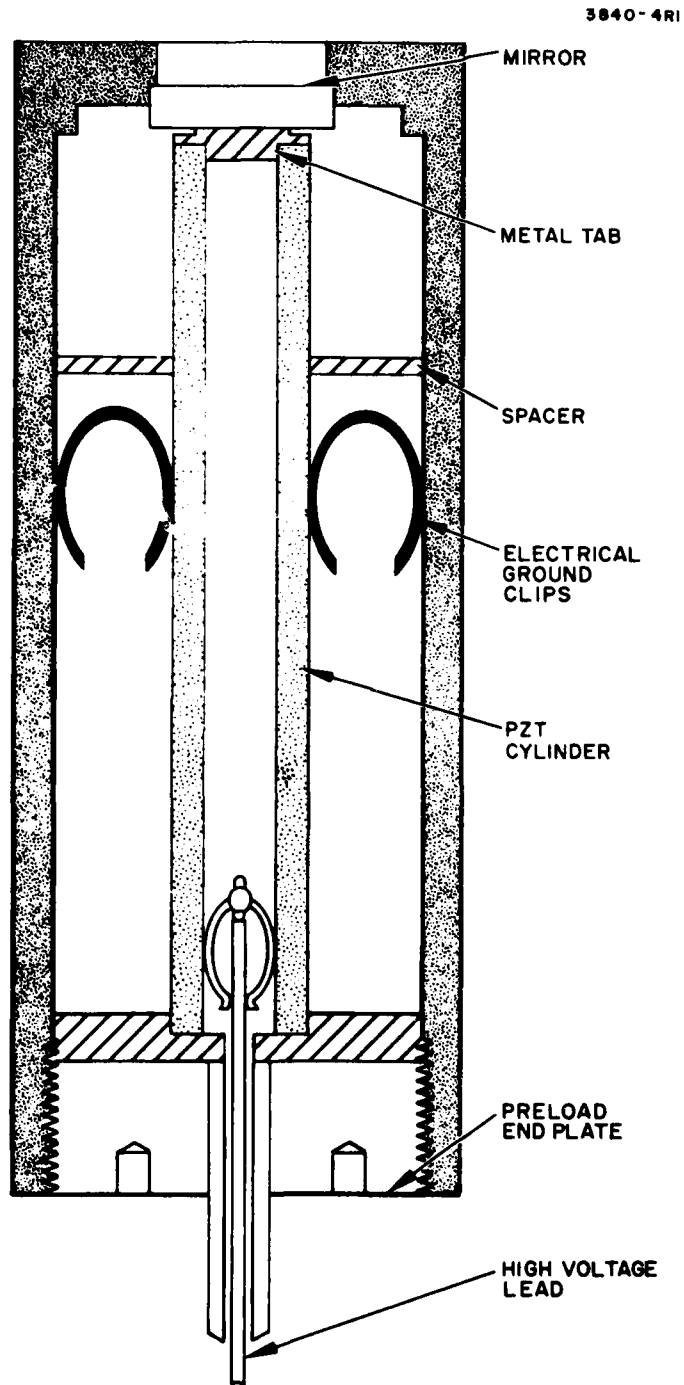


Figure 26. Piezoelectrically-driven, variable-radius spherical mirror used for autofocus control.

frequencies shown in Table 7, although sine/cosine operation with the 19-element system has been demonstrated (using the phaser matrix).

The design of the servo electronics was optimized using a computer simulation. The parameters studied included the number and corner frequency locations of high-pass and low-pass filters, dither frequencies and spacings, minimum signal-to-noise ratio, open-loop gain, and dither amplitude. The final values used include a five-stage low-pass filter as listed in Table 8.

The primary differences between the electronics now employed for the deformable mirror and the previous phaser matrix are the control channel driver and the dither injectors. These are discussed below.

#### Control Drivers

The control channel drivers provide the high voltage necessary to drive the PZT actuators in the deformable mirror. The input level to the drive is compatible with standard  $\pm 15$  V operational amplifier output voltages. The output section of the amplifier is made up of a high-voltage quasi-complementary transistor pair biased by a constant current source. Cross-over distortion and thermal instability are compensated for by using matched diodes in conjunction with the biasing circuitry. The output transistors are over-current protected to 25 mA to prevent possible damage, with an output capability of  $\pm 150$  V and a 25-mA current limit. The maximum power dissipation is 7.5 W.

#### Dither Injector

In the present COAT system employing one deformable mirror, the dither drive signal and the control drive signal are combined to drive a single actuator. A high-Q ferrite core transformer is used to inject the dither signal onto the low-frequency, high-voltage control signal. By using the injection technique, the bandwidth-limited high-voltage control driver does not have to drive the mirror actuator at dither frequencies. The injection transformer performs three functions: It insulates the low voltage dither circuitry from the high voltage control coming from the control driver; it allows low-voltage high-power transistors to be used in the dither driver design; in effect, it extends the usable dynamic range of the high-voltage control driver because the dither signal is added in series with the control voltage and is not affected by the saturation of the control driver.

TABLE 7. DITHER FREQUENCIES FOR  
19-CHANNEL COAT SYSTEM

---

|                          |                             |
|--------------------------|-----------------------------|
| $f_1 = 8.2 \text{ kHz}$  | $f_{10} = 20.8 \text{ kHz}$ |
| $f_2 = 9.6 \text{ kHz}$  | $f_{11} = 22.2 \text{ kHz}$ |
| $f_3 = 11.0 \text{ kHz}$ | $f_{12} = 23.6 \text{ kHz}$ |
| $f_4 = 12.4 \text{ kHz}$ | $f_{13} = 25.0 \text{ kHz}$ |
| $f_5 = 13.8 \text{ kHz}$ | $f_{14} = 26.4 \text{ kHz}$ |
| $f_6 = 15.2 \text{ kHz}$ | $f_{15} = 27.8 \text{ kHz}$ |
| $f_7 = 16.6 \text{ kHz}$ | $f_{16} = 29.2 \text{ kHz}$ |
| $f_8 = 18.0 \text{ kHz}$ | $f_{17} = 30.6 \text{ kHz}$ |
| $f_9 = 19.4 \text{ kHz}$ | $f_{18} = 32.0 \text{ kHz}$ |
|                          | $f_{19} = 33.4 \text{ kHz}$ |

---

T1117R

TABLE 8. COAT SERVO DESIGN VALUES

- 
1. Minimum dither frequency spacing,  $\Delta f = 1.4 \text{ kHz}$ . Smaller  $\Delta f$  requires lower loop gain for stability; lower gain gives slower response.
  2. Low-pass filter: 1 stage at  $f = 10 \text{ kHz}$ , 4 stages at  $f = 5 \text{ kHz}$ .
  3. High-pass filter: 1 stage at  $f = 1 \text{ kHz}$ , 1 stage at  $f = 170 \text{ Hz}$ .
  4. Dither amplitude  $= \pm 20^\circ$ .
  5. Maximum open loop gain  $= 38 \text{ dB}$ .



The dither signal from the secondary of the step-up injection transformer is dropped across a voltage divider consisting of the low-pass filter capacitor in the output of the control driver and the capacitance of the PZT. The frequency range of the dither driver driving a 0.022  $\mu$ F PZT actuator to 50 V peak-to-peak is approximately 2 to 60 kHz at the 3-dB points.

#### OPTICAL SYSTEM DESCRIPTION

The details of the optical arrangement differ depending upon the experiment in question. For the particular set of performance experiments to be discussed below used in "Performance Characteristics," the arrangement employed is shown in Figure 27. There are two optical paths, one known as the "local loop," which is an undistorted path, and a propagation path where turbulence or blooming distortions can be introduced.

When photomultiplier (PMT) 1 is connected to the COAT servo system, a diffraction-limited beam is produced at target plane 1. In addition, this beam is put into the path containing the auxiliary tracking and focus controls and any distortions that are introduced. The Strehl ratio with no COAT correction is measured in this way. When PMT 2 is connected to the COAT servo system, the performance of the deformable mirror plus the auxiliary tracking and focus controls can be ascertained. In particular, the degree of COAT correction is measured by switching PMT 2 into the servo system.

The diagnostics employed to analyze the system performance depends upon the experiment in question. In general, it consists of TV monitoring, x-y chart recordings, and pinhole photodiode detectors. For the experiments discussed under "Performance Characteristics," the particular diagnostic arrangement used will be described as necessary.

The particular set of optical elements shown in Figure 27 were chosen based on availability of lens, desired spot size in the far field, distance to the far field, and beam size requirements for the focus mirror and the micro-slewing tracking mirrors.

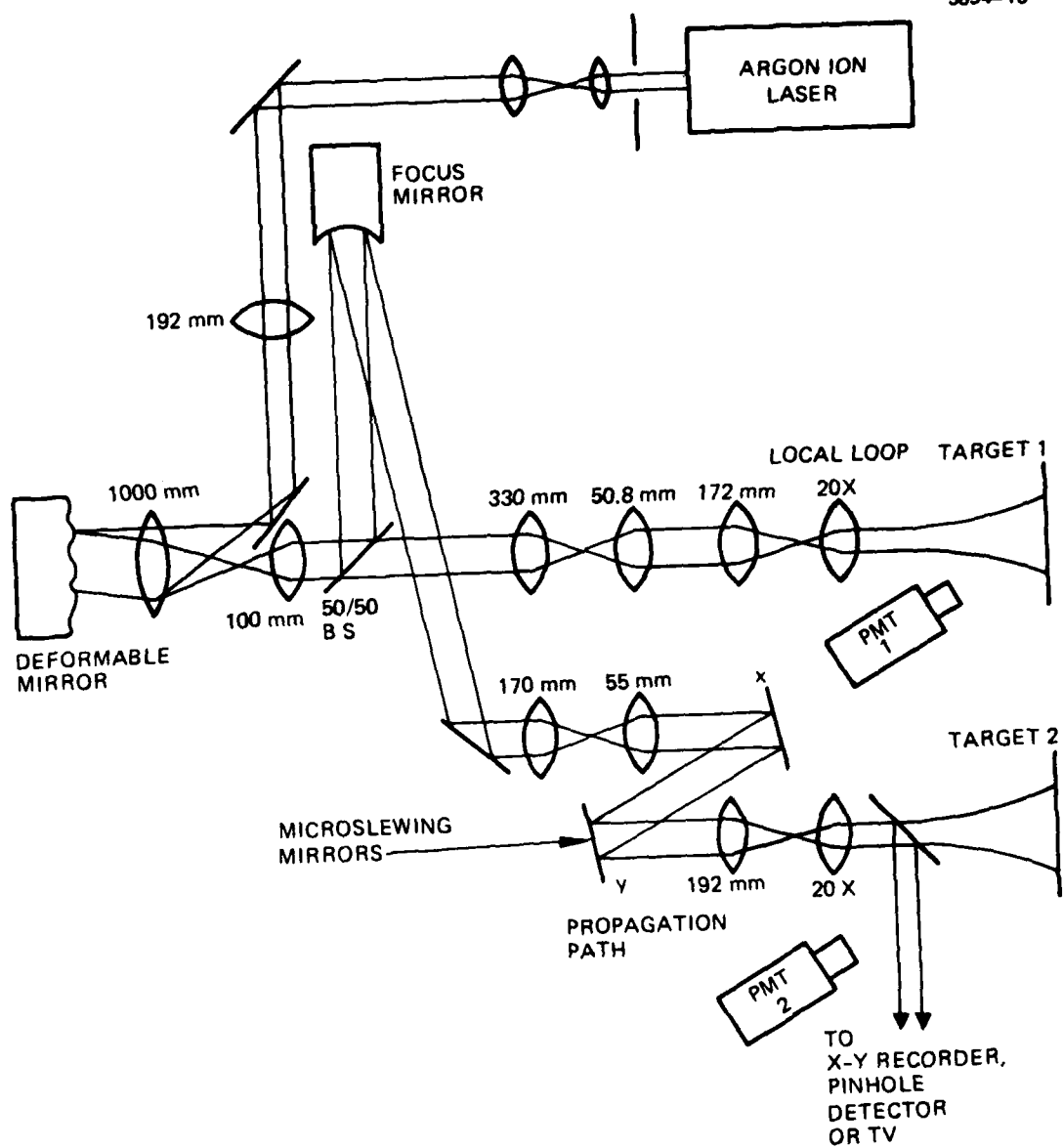


Figure 27. Optical arrangement.

## MIRROR/ELECTRONICS COMPATIBILITY

Due to the variations in actuator sensitivity, phase shift and mechanical resonances, the deformable mirror must rely on the flexibility of the COAT electronics to provide proper compensation.

The need to compensate for large phase variations becomes apparent when the deformable mirror is operated near its resonant frequencies. The COAT electronics can provide an adjustable phase shift of up to  $360^\circ$  by using the two internal  $0$  to  $180^\circ$  phase shifters located on the oscillator boards (Figure 22(b), blocks 3,4). The signal that goes to the dither driving circuitry (Figure 22(b), blocks 6,7) also goes to the phase shifters to the "Y" input of the analog multiplier (Figure 22(b), block 1). The phase shifters are adjusted so that the signal that is fed to the "Y" input of the multiplier arrives with the same phase as the received dither signal. The effects of the mirror, the driving electronics, and the delay caused by range propagation are all removed by adjusting the phase shifters properly.

Operating the mirror near resonances causes greater excursions for a given drive level. Therefore, the dither amplitudes have to be individually adjusted for each channel (Figure 22(b), block 6) to give a constant signal amplitude from the receiver. This adjustment also compensates for the lower light level from the outer mirror actuators due to the normal gaussian power distribution. The AGC in the present COAT system (Figure 22(a), block 7) functions on dc or average light levels received by the photomultiplier and does not adjust gain on an individual channel basis. Maintaining the received dither amplitudes at a constant level insures that gain variations among the channels are minimal and that the AGC in the signal conditioning electronics can function most efficiently.

The control signals, which are below 400 Hz and far below the mirror resonances, are treated as dc and can be adjusted using an interferometer. By using the two-hole aperture mask as discussed before, a two-element interferometer is formed. One of the two actuators is then used as a nondriven reference while the driven actuator produces the fringe movement and an indication of actuator sensitivity. The control drivers are driven to their full positive and negative excursions. The channel with the smallest fringe movement is used as a gain-setting reference for the other control channels.

## PERFORMANCE CHARACTERISTICS

This section presents a description of the experiments performed to establish the basic operating characteristics of the deformable mirror COAT system. The experiments described do not involve tests with thermal blooming or with turbulence levels other than that occurring in the laboratory. Thermal blooming compensation studies are to be conducted during the remainder of this contract and will be discussed in the final report.

### COAT System Gain-Phase Measurements

Classical servos can be evaluated by open- and closed-loop gain-phase plots, which are interpreted to determine gain and phase stability margins. The RADC COAT System was evaluated in 1974 with its original phasor matrix installed and the results were published in 1976.<sup>3</sup> These same electronics have been combined with the new deformable mirror and the measurements repeated. The open-loop results are shown in Figure 28, and are very similar to the previously published results. Loop voltage gain was adjusted to 30 dB. The measured phase margin is 75°; the gain margin is -12 dB.

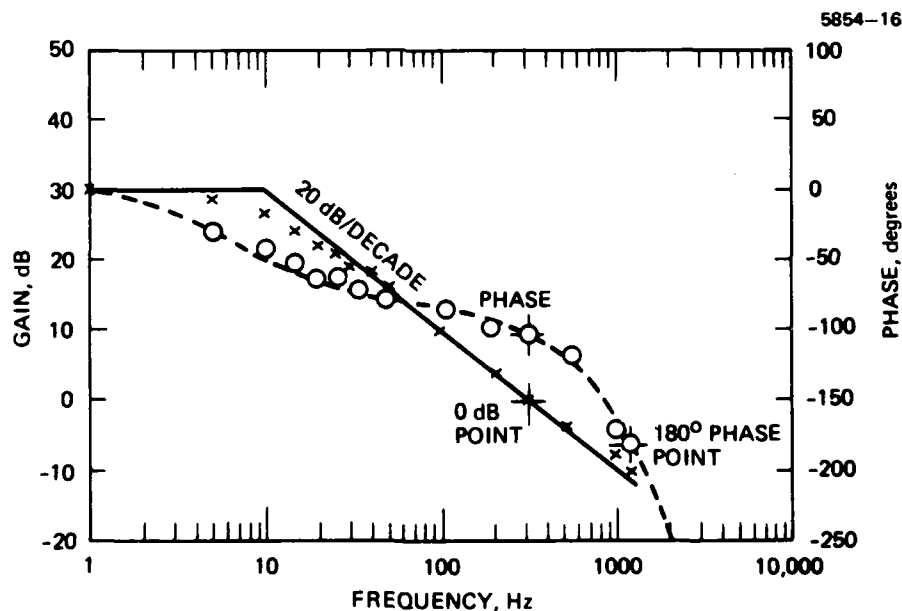


Figure 28. Open loop gain/phase measurements 19 channel RADC mirror.

Closed-loop measurements were hampered by restricted dynamic range and nonlinearities introduced by the symmetrical clipper preceding the analog multipliers (synchronous demodulators), and are not shown here. The difficulty was caused by the need to increase loop gain to compensate for the lower sensitivity of the deformable mirror relative to the phasor matrix. The only readily accessible control for loop gain is a post-amplifier following the AGC amplifier, but preceding the clipper. The best place to increase the gain would have been in the dc amplifier/filters following the synchronous detectors, but adjustments of gain at that point require hardware modifications of the 19 individual channels, and it was not attempted due to the short time available for the measurements program.

After completion of the gain-phase measurements, the clipping level of the symmetrical clipper was changed to eliminate the large-signal nonlinearity, and convergence times compatible with the 300 Hz bandwidth (1.5 msec) were achieved (see below). If schedule permits, the closed-loop gain-phase measurements will be repeated, but the correlation of the open-loop measurements and the convergence time make these measurements redundant, thus they have a low priority.

#### Convergence Time

The convergence time is obtained from temporal profiles of the PMT intensity following closure of the COAT servo electronics loop. One such profile is shown in Figure 29. The COAT-ON scope trace begins when the COAT servo loop is closed. The other traces are the baseline, PMT blocked, and the PMT intensity with COAT OFF. For this case, the system converges from its initial to final state in about 1.5 msec. This convergence time varies from one loop closure to the next depending on the initial conditions. This can be seen in Figure 30 where the initial conditions were varied by moving the glint known distances from the boresight of the laser. (All this data is obtained using the local loop.) Plotted in Figure 30 are the convergence time, the absolute intensity level achieved by the PMT, and the ratio of the PMT COAT-ON intensity to the COAT-OFF intensity as a function of distance from boresight. With COAT OFF, the beam pattern has a maximum intensity at the boresight and minimums as you proceed from the boresight. These points are marked on the plot. From this data it appears that

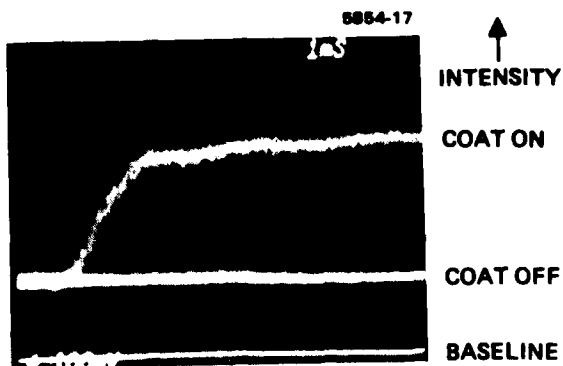


Figure 29.  
Convergence time of COAT  
system.

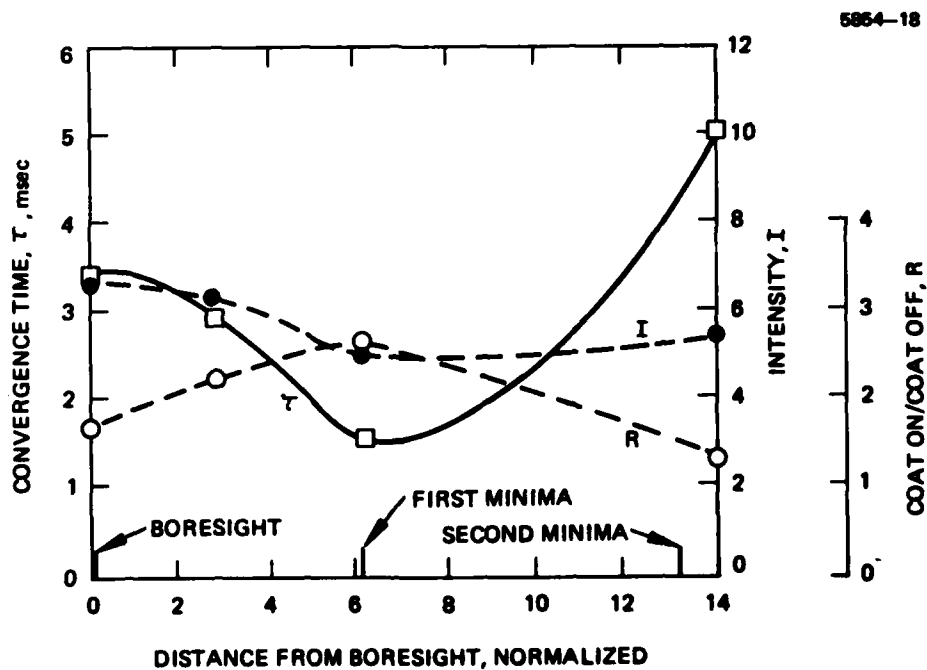


Figure 30. COAT performance.

the convergence time passes through a minimum depending upon the distance from the boresight or, equivalently, the magnitude of the initial intensity. Qualitatively, this can be explained as follows: With large initial signal the open-loop gain is low, hence a lower frequency crossover point with the zero gain closed-loop condition (zero dB point on Figure 28), thus a slow rise time. As the initial signal decreases, the gain becomes larger, leading to a higher-frequency zero dB point and a faster risetime, as seen at the first minimum. As the initial signal is decreased further, out to the second minimum, the control error begins to exceed the capability of the mirror excursion for some actuators and the system again slows down. From this data the ratio of COAT-ON-to-COAT-OFF intensity peaks at the initial condition to give the fastest rise time. Further, the PMT intensity with COAT ON is nearly constant independent of initial condition with a slight minimum occurring at the point of fastest rise time.

#### Beam Formation

Beam formation data was obtained for various cases of initial defocus. Strehl ratios approaching 80% were obtained for defocus conditions as large as an order of magnitude. A typical beam profile achieved is shown in Figure 31. Here the COAT-OFF and -ON signals are shown for about a factor-of-5 defocus with no turbulence. A chart recording of the formed array pattern for this case is shown in Figure 32. This data is obtained by attaching a 0.01 in. pinhole photodiode detector to the arm of an x-y chart recorder and recording the resulting profile.

It is important to distinguish between PMT intensities and peak irradiance on target obtained from pinhole photodiode measurements. The magnitude of the initial PMT intensity from which the COAT system converges is an important parameter for systems where the receiver is located near the laser, such as Annular Aperture Impact or Shared Aperture Impact schemes.<sup>4</sup> The effect of decreasing this initial level was studied in the present set-up by inserting filters in front of the receiver PMT. For one state of defocus (factor of 10), the relative convergence was then obtained as a function of this initial level. The results are shown in Figure 33. It is seen that even for a two-order-of-magnitude decrease in signal, the convergence level only drops to about 82% of the original value.

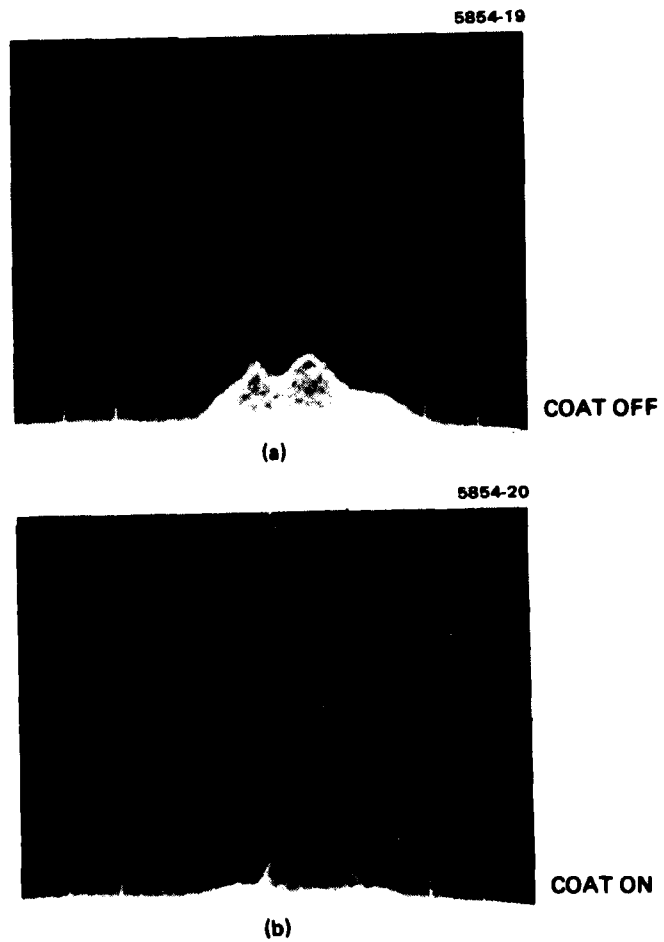


Figure 31.  
Beam profile (a) COAT-OFF, beam defocused  
(b) COAT-ON; no turbulence.



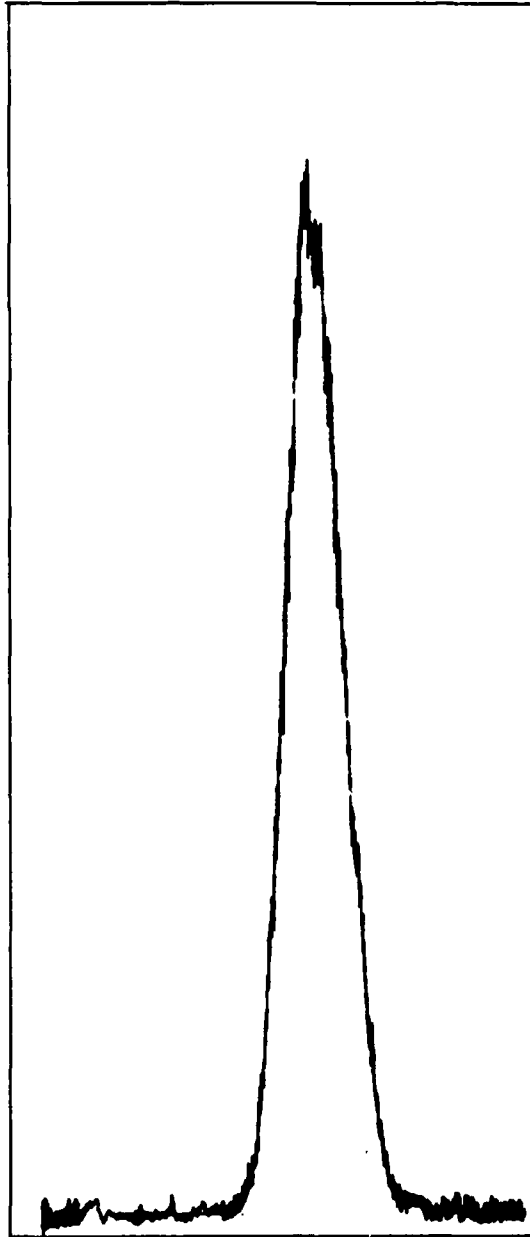


Figure 32. Formed array pattern;  
no turbulence.

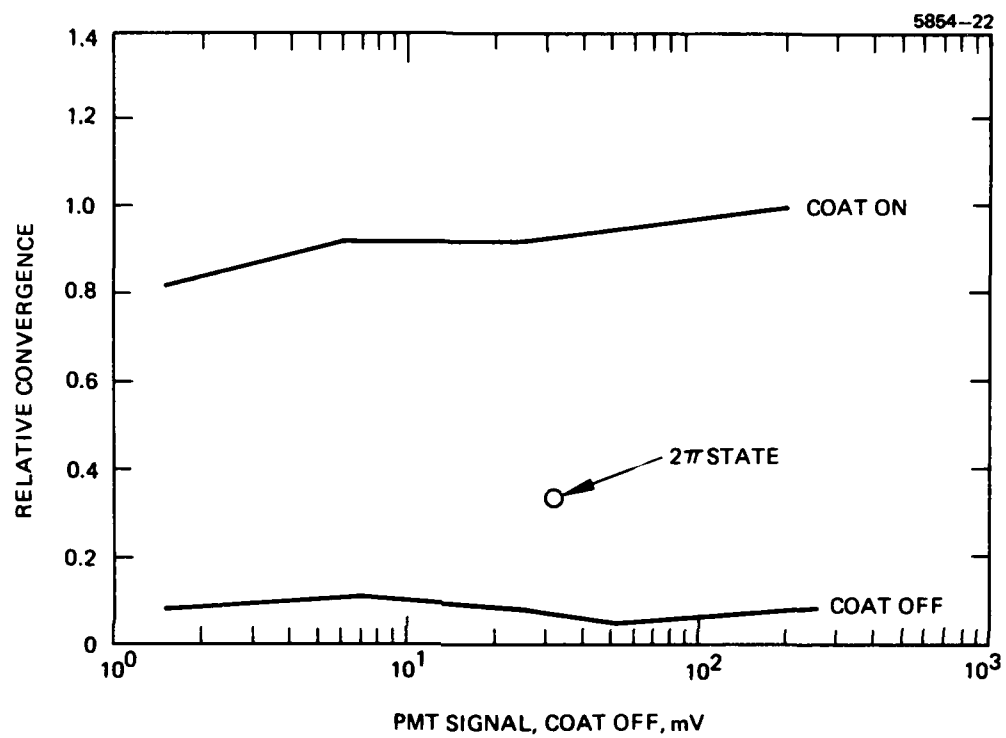


Figure 33. Relative convergence as a function of PMT signal level.

The deformable mirror has the capability to track a glint over a limited dynamic range. This tracking ability is shown in Figure 34. Here the glint is positioned on the pinhole detector and moved through the beam as shown. Comparing this figure to Figure 32 establishes that the mirror can track about 3 to 4 diffraction-limited beam diameters in length. An interesting aspect of this data is the sudden jump in intensity, of almost a factor of two, that occurs nearly half-way through the trace. This is speculated to be due to a  $2N\pi$  state. This will be discussed more fully below.

#### Operation with Auxiliary Track and Focus Controls

A large number of tests were run using the auxiliary tracking and focusing controls with the deformable mirror. One of the difficulties of using these auxiliary systems is that no AGC is included in their servo systems, thus a manual adjustment of the gain is required for optimum convergence.

An oscilloscope trace of target irradiance versus time is shown in Figure 35 for the tracking servo. From this data the convergence time is about 10 msec. This is expected because of the slower dither system. The convergence time of the focus control was found to be about 100 msec as expected (data not shown). To test the focus servo, the system was defocused such that a doughnut intensity profile was obtained and various convergence data taken. Figure 36 shows the PMT intensities for the various cases. Figure 36(a) is for the initial condition of FOCUS OFF and Figure 36(b) is for FOCUS ON. When COAT is subsequently turned ON, the result is an improvement in PMT signal by a factor of two. However, the final converged power on the target did not improve:

| <u>Case</u>       | <u>NO FOCUS</u> | <u>WITH FOCUS</u> |
|-------------------|-----------------|-------------------|
| ALL OFF           | 0.003           | 0.003             |
| FOCUS ON          | —               | 0.016             |
| COAT ON           | 0.274           | —                 |
| COAT and FOCUS ON | —               | 0.267             |

This data is pinhole detector data of peak target irradiance. The key point is that the numbers in the table represent long time results. It was found that



Figure 34. Deformable-mirror tracking of a moving glint; no turbulence.

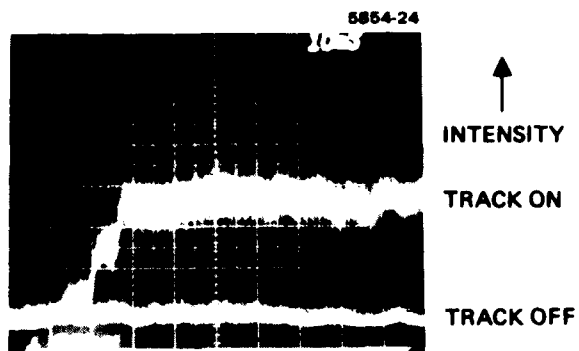
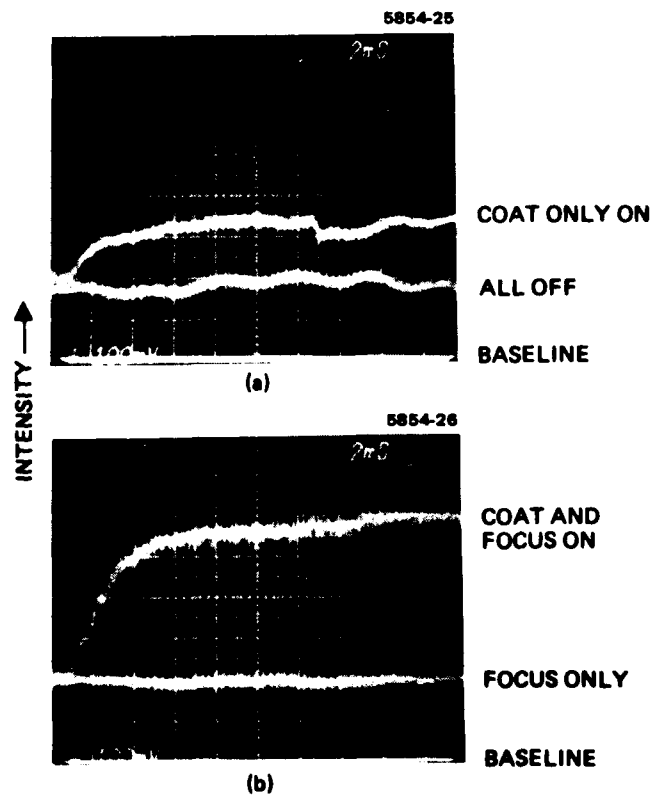


Figure 35.  
Convergence time of tracking  
controls.

Figure 36.  
PMT levels for (a) initial  
level — no focus; (b) initial  
level — with focus.



the FOCUS-ON case intensity rose immediately to the 0.267 value whereas the FOCUS-OFF case required a considerable time (approximately minutes) to reach its final state. Thus the PMT data of Figure 36(a) is just an intermediate state (possible  $2N\pi$  state) before the final state is reached corresponding to the Figure 36(b) results. This was verified by observing long-time chart recording data of the FOCUS-OFF case.

The performance of the tracking system is shown in Figure 37. The start and finish of these traces is artificial due to the method by which the data was taken. In fact, the tracking would continue as long as the glint was in the field of view of the PMT (which was stationary).

An interesting effect is seen in this tracking data (not observed with the previous phasor matrix and tracking data). After tracking a certain distance the system appears to unlock, track at some lower value and lock up into a higher state again. This is probably due to lock-up into a  $2N\pi$  state during the tracking period.

#### $2N\pi$ Ambiguities

The ability of a deformable-mirror multidither system to lock up in a non-optimum  $2N\pi$  state has been discussed in detail by O'Meara.<sup>2</sup> Briefly, the  $2N\pi$  problem occurs because each channel in the deformable-mirror dither system has multiple zero-error states of the servo that occur whenever the optical phase error in that channel is roughly a multiple of  $2\pi$ . The maximum target irradiance occurs only for zero phase error, however. Depending on the state of the neighboring mirror actuators (control channels) and the influence function, a  $2N\pi$  condition in a given channel can be either an unconditionally stable state or a marginally unstable state where the servo has a finite error signal, but very low gain. In the second case, the servo will drive the channel phase error toward zero, but at a greatly reduced rate from the nominal small-error servo convergence rate. In effect, the  $2N\pi$  condition reduces greatly the control bandwidth in the affected channel. From the data presented previously, the evidence for the existence of these states is shown. In particular, in Figure 34 the sudden jump in intensity is one example; in Figure 33 one data point is shown with an intensity well below that achieved most of the time (this is speculated to be a  $2N\pi$  state) and finally, the tracking data shown in Figure 37 also illustrates the same condition.

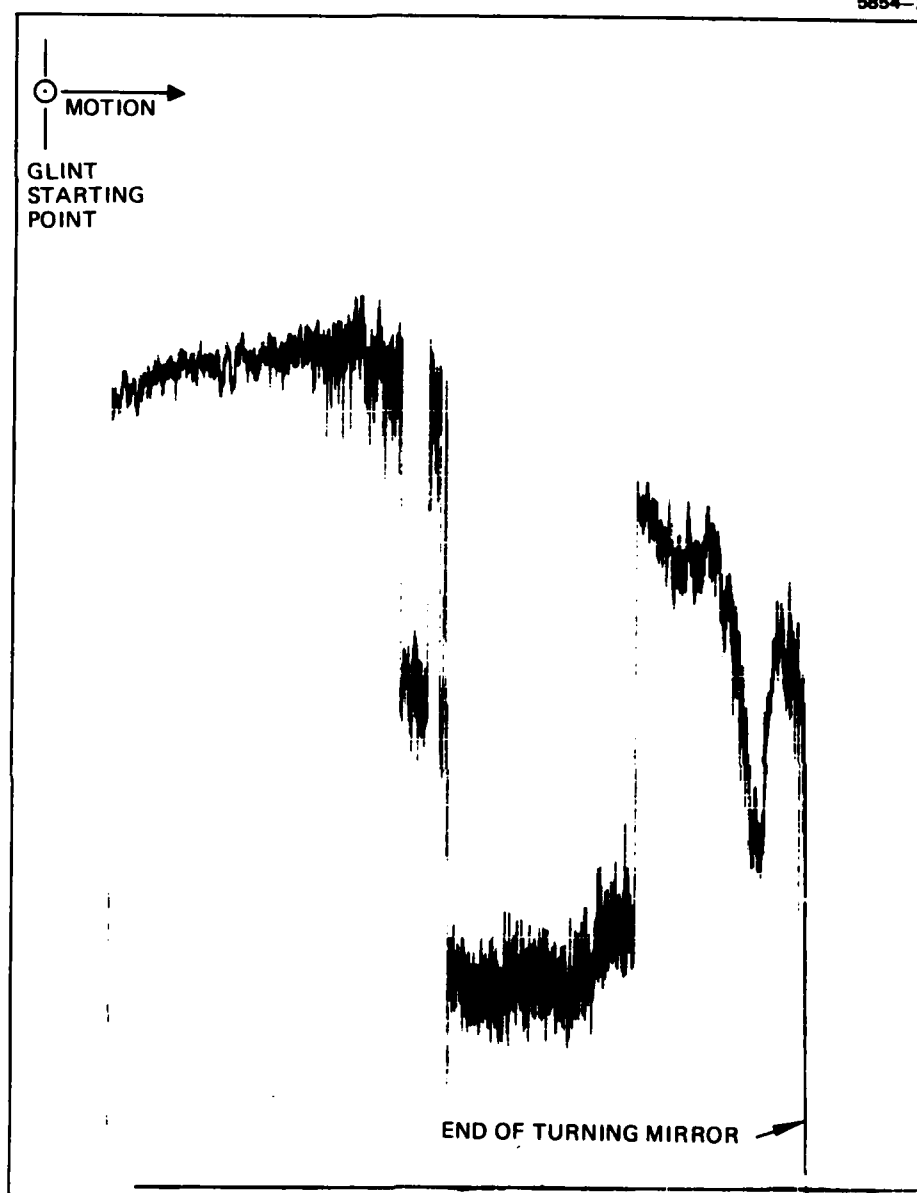


Figure 37. Deformable mirror plus auxiliary tracking performance.

Testing on other deformable mirrors at HRL has shown the existence of irradiance fluctuations in turbulence compensation studies thought to be caused by  $2N\pi$  states (see Figure 38 which was taken from Pearson and Hansen<sup>5</sup>). Figure 38 shows several time records of the error signal in a single servo channel. The channel observed drives an actuator near the edge of the mirror and thus is more likely to encounter a  $2\pi$  error. The fast transitions of over  $2\pi$  in phase shift, indicated by arrows in Figure 38, were attributed to the channel dropping out of a  $2\pi$  lockup state. The transitions occurred in roughly 4 to 10 msec, which is comparable to the servo system convergence time, and were thus thought to be too rapid and too large in amplitude to be caused by the servo responding to normal atmospheric turbulence errors.

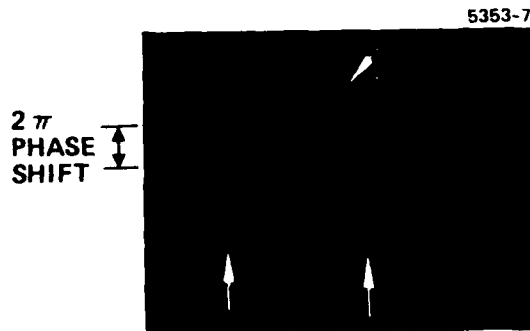
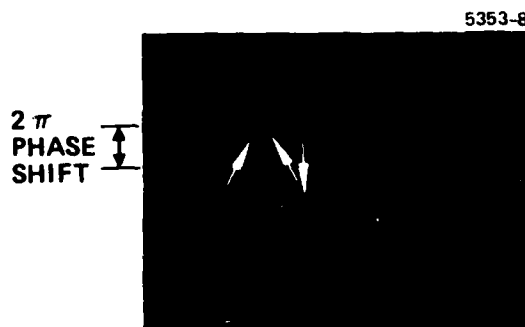


Figure 38.  
Servo error signals occurring in  
a single COAT control channel  
under conditions of high turbu-  
lence (from Pearson and Hansen<sup>5</sup>).





These data demonstrate the existence of  $2N\pi$  lockup states in deformable-mirror multidither COAT systems and also illustrate how detrimental they can be to system performance. Clearly, optimum performance from a deformable-mirror multidither COAT system will be possible only when these detrimental effects can be removed or minimized. Numerous candidate techniques for alleviating the problem are under study. Any successful techniques, however, must be able to distinguish between a  $2N\pi$  servo-lockup error and a desired  $2N\pi$  phase shift. Thus a simple limiting of actuator excursion to less than  $2\pi$  of phase shift will eliminate  $2\pi$ -lockups, but will also severely limit the error-correction dynamic range. Another simple technique is to limit the mirror actuator excursion between adjacent actuators to less than  $2\pi$  phase shift. This technique limits the local wavefront error slope correction, which may not be an unduly severe restriction in many cases of interest. The technique has a further difficulty, however, because a  $2N\pi$ -lockup occurs whenever the difference between the existing mirror state and the instantaneous wavefront error is  $2N\pi$ . In principle, a  $2N\pi$ -error condition could thus occur with a flat mirror. In addition, this technique will not rapidly relieve the "block"  $2N\pi$  problem discussed by O'Meara.

## HIGH POWER ASSESSMENT

Although the RADC deformable mirror was designed and fabricated as a low-power, uncooled assembly, the applicability of incorporating its basic design features in a high-power, cooled mirror were evaluated. These considerations included mirror performance, material properties and fabrication techniques. Required faceplate excursions and operating bandwidths were the same as for the present mirror. Since the present mirror is constructed of beryllium, and most high-power mirrors are constructed of molybdenum, most of the assessment is based on the use of one or both of these materials.

### FABRICATION AND MATERIALS

In selecting a material or fabrication method to be employed in any deformable mirror, the following considerations must be applied:

- Performance required of that component
- Preferred physical and mechanical properties
- Manufacturing options available
- Environment in which the component is used
- Techniques available for installing the material into the mirror structure
- Compatibility of the material with other materials in the mirror
- Material fatigue limits commensurate with high reliability.

A high-power deformable mirror is subjected to a severe thermal and mechanical environment and is required to maintain optical tolerances. This imposes unique requirements on the materials.

#### Heat Exchanger Considerations

Thermal loads and heat exchanger performance of deformable mirrors are similar to those of conventional optics, but the thermal effects are different. The principal distortions of conventional high-power cooled mirrors are first-order beam mapping extension of the faceplate and support column field, thermally-induced intercolumn Poisson rippling, and backup structure

bending caused by rise in coolant temperature. In deformable mirrors, interactuator thermal bowing of the faceplate assembly supplants backup structure bending, while beam mapping distortions are strongly influenced by faceplate stiffness requirements.

The faceplate assembly, which is heated by the beam and must bend to permit phase correction, is best suited to a material with a high thermal conductivity and a low modulus of elasticity. Copper, which possesses these properties, would appear to be a good candidate; however, our experience has shown copper to be a poor material for optical elements. It is difficult to obtain a good optical finish on copper surfaces. Also, the low modulus of copper combined with its high ductility results in a material which does not maintain an optical figure. Both beryllium and molybdenum have been used extensively by Hughes in the fabrication of high-quality optical elements. Each of these materials has a relatively high thermal conductivity and a high modulus of elasticity. The disadvantages of the increased stress and force required in the deflection of faceplates constructed of these high-modulus materials is offset by the reliability and optical stability of the resulting structure. Molybdenum offers a further advantage due to its low coefficient of thermal expansion, which is less than one half that of beryllium. The lower coefficient of thermal expansion yields lower thermally-induced stresses and distortions.

#### Mirror Body Considerations

The mirror body or backup structure must provide the optical reference for the faceplate and the fixed point from which the actuators derive their motion. In a deformable mirror the natural frequency of this structure is a primary concern. The natural frequency of a deformable mirror may be increased significantly through appropriate selection of backup structure material and thickness.

For relatively thin circulator plates, the equation describing the fundamental frequency is of the form:

$$f_n = \sqrt{K \frac{E}{\rho} t}$$

where

$f_n$  = natural frequency, Hz

$K$  = geometrical constant

$E$  = Young's modulus, psi

$\rho$  = density, lb/in.<sup>3</sup>

$t$  = thickness of mirror, in.

As can be seen, for thin mirrors, the natural frequency is proportional to  $t$ . As the mirror tends to become thick, shear effects are more pronounced and there is less dependency on  $t$ . The natural frequency is proportional to  $\sqrt{E/\rho}$ , (specific stiffness) being a function of material only. Beryllium has one of the highest known specific stiffness. Thus beryllium is a highly desirable backplate material. Based on the preceding, a beryllium structure, all other things being equal, yields a natural frequency 2.26 times that of a molybdenum structure.

As a mirror becomes more complex, the equation given for the natural frequency becomes less and less valid. For deformable mirrors, the equation is useful only for rough estimation of the relative effects of thickness and specific mirror on structural analyzer computer programs, such as is necessary to set the accurate mode frequencies and shapes.

#### Fabrication Considerations

Machining. Almost all standard machining operations which are applicable to other metals can be accomplished with beryllium and molybdenum. Due to the metallurgical characteristics of these materials, the necessity for tapping fine threads should be minimized. Other than the restriction on fine threads, the design options available with most other metals are available with these materials. However, both materials require special care during any machining operation. All beryllium parts must be subjected to a special thermal-stress relief cycle following machining operations. This process is necessary to remove the stresses and notches developed at the surface during cutting operations.

Joining. Ideally an optical element should be constructed from a single piece of homogenous material. Since this is not possible in these types of deformable mirrors, joining techniques which approximate a homogenous structure

are required. To retain good optical figure, a permanent, optically-stable joint is required at all interfaces. Molybdenum mirrors have been joined by brazing; techniques have been developed for brazing these mirrors which yield optically stable structures. Tests have shown them to maintain optical figure even when cycled over a temperature range of  $-40^{\circ}\text{F}$  to  $+200^{\circ}\text{F}$ . Beryllium mirror structures have been brazed successfully with both silver and aluminum brazing alloys. Molybdenum and beryllium may also be joined by various bonding techniques. However, our experience has indicated that most bonded joints do not have the reliability and stability of brazed or mechanical joints.

### LIMITATIONS

The preceding discussions have indicated the viability of a high-power mirror constructed of either molybdenum or beryllium. However, there are limitations imposed by each material that should be considered. A high-power mirror necessitates the pumping of a liquid coolant, usually water, through the heat exchanger assembly and manifolds in the mirror body. This requires that the structure not be susceptible to corrosion from these coolants. Also, a deformable mirror is subjected to dynamic as well as static stresses. Stress limits in the materials must be evaluated. Finally, the difficulties and problems associated with the various manufacturing techniques require consideration. The following discussions address these concerns for both molybdenum and beryllium mirrors.

#### Corrosion

Molybdenum offers excellent corrosion resistance in the presence of water and most liquids. Due to the electrolysis developed between molybdenum and the brazing alloy, the use of electrically nonconductive liquids in the mirror structures is preferred. Deionized water has served very well as a mirror coolant, and alleviates galvanic corrosion at the braze joints. Beryllium does not offer the corrosion resistance that may be obtained with molybdenum. Preliminary tests of beryllium heat exchanger samples with deionized water have shown no corrosion problems due to oxidation or galvanic corrosion.

However, these tests are not considered to be adequate to predict the reliability of a beryllium heat exchanger assembly. The beryllium and its braze alloys have a greater electromotive potential than the molybdenum and its braze alloys.

#### Stress Limits

Molybdenum and beryllium both offer excellent structural properties. Since the deformable mirror is subjected to repeated and reversed cycling of loads, a conservative stress limit is applied. Table 9 gives the stress limits for each material. The fatigue limits shown in Table 9 are based on published values. The fatigue stress limit for molybdenum is based on an unlimited number of repeated and reversed cyclic loadings; whereas, the beryllium limit is based on  $10^6$  cycles.

#### Manufacturing

Although most fabrication techniques are applicable to both molybdenum and beryllium, the availability of facilities for machining and brazing beryllium is limited. Molybdenum may be machined in almost any facility which has experience in machining refractory metals. However, beryllium requires special facilities to provide the safety requirements imposed for the toxic particles removed during machining. Hughes, as well as many other companies, has in-house facilities and considerable experience in brazing molybdenum. There are only a few sources in this country with the facilities and the expertise for brazing beryllium. Thus, manufacturing schedules and costs are typically greater for parts constructed from beryllium.

TABLE 9. MATERIAL STRESS LIMITATIONS

|            | Ultimate Stress, psi | Yield Stress, psi | Fatigue Stress Limit, psi |
|------------|----------------------|-------------------|---------------------------|
| Beryllium  | 35,000 to 110,000    | 25,000 to 82,000  | 35,000                    |
| Molybdenum | 100,000              | 68,000            | 45,000                    |

## SUMMARY OF DESIGN APPLICABILITY TO HIGH-POWER COOLED MIRRORS

The basic design concept employed in the RADC deformable mirror is applicable to a high-power mirror design. The design changes required to accommodate high-power applications are: Replacement of the existing 0.125-in. thick faceplate with a cooled heat exchanger of comparable stiffness, and modification of the mirror body to accommodate manifolding to port the coolant to and from the heat exchanger assembly. Hughes has designed and manufactured cooled deformable mirrors which incorporate each of the features. The basic difference in these mirrors and the RADC mirror design is the use of beryllium as the mirror material.

Beryllium can be used in the manufacture of the RADC mirror design for high-power application, and offers a distinct advantage. The large  $E/\rho$  of beryllium yields a maximum resonant frequency for a given mirror design. The low density also provides the lightest overall mirror weight. The present RADC mirror body weighs only 2.6 pounds. A similar mirror constructed of molybdenum would weigh six times this value.

However, the fabrication difficulties and long schedules incurred during the manufacture of the RADC mirror encourage the use of a molybdenum mirror. Also, the corrosion difficulties expected to result from the coolant in contact with the beryllium and the braze joints has a considerable impact on the reliability of a water-cooled beryllium mirror.

Hughes has proposed designs previously which take advantage of the preferred properties of both beryllium and molybdenum. Further studies are required before they could be incorporated in a mirror design. Molybdenum mirror designs presently being tested are showing performance characteristics similar to those of the RADC mirror. Thus, it is possible to achieve the RADC mirror performance in a similar mirror constructed of molybdenum; some modification to the design details would be required.

## PLANS FOR REMAINDER OF CONTRACT

The final phase of the contract will be devoted to detailed experimental investigations of thermal blooming compensation. In addition, analytic studies of various algorithms for thermal blooming will be pursued. The experimental program will use both the standard zonal multidither system and Zernike polynomials to study thermal blooming compensation.



## REFERENCES

1. J.E. Pearson, S. Hansen, M.L. Minden, C. Yeh, "Multidither adaptive algorithms, Dec 1975 and Sept 1976.
2. T.R. O'Meara, "Multidither COAT systems operating with deformable mirrors," submitted J. Opt. Soc. Am.
3. J.E. Pearson, et al., Appl. Opt., Vol. 15 No. 3, Mar '76, p. 616.
4. J.E. Pearson, S. Hansen, T.R. O'Mara, "Adaptive control over extended targets," Interim Technical Report, Sept. 1976.
5. J.E. Pearson and S. Hansen, "Experimental studies of a deformable mirror multidither COAT system," submitted to J. Opt. Soc. Am.

PRECEDING PAGE BLANK-NOT FILMED

## APPENDIX I

### MIRROR PROFILE MEASUREMENTS

#### INTRODUCTION

Deformable mirrors are used for introducing phase corrections in the optical path of a telescopic system. A deformable mirror consists of a thin disc whose front surface is finished as a mirror and whose rear surface is attached to an array of electromechanical actuators capable of deforming the mirror surface in a controlled manner.

The response of a deformable mirror to signals applied to its actuators will be frequency-dependent in a complex manner, but in a typical design using piezoelectric actuators, the mass-to-stiffness ratio is such that response will be essentially constant from dc up to some frequency well in excess of 1 kHz. In this range, the mirror can be characterized by measuring the surface profile resulting from unit signal applied to each actuator in turn while the others are short-circuited. These profiles are all influenced by the proximity of the mirror edge and as a result will differ from one another to a significant extent.

A useful idealization for performance analysis can be made by neglecting edge effects and assuming that the local unit profile associated with each actuator is the same for all actuators. The usual practice is to measure the profile of the center actuator, which is least affected by the mirror edge. A mathematical approximation to this profile is then taken to be the unit profile for all actuators in a computer simulation.

#### MEASUREMENT METHODS

Mirror profiles can be measured either optically or mechanically. In the past, profiles have usually been measured by classical interferometer techniques. The accuracy and resolution obtained in this way have been poor for two reasons. First, the total mirror excursion is small and may only be one or two wavelengths of the incident radiation. Second, as usually performed, it is a quasi-dc method and may be influenced by the hysteresis of the actuator.

DATE  
FILMED  
- 8